TOI-1431b/MASCARA-5b: A Highly Irradiated Ultrahot Jupiter Orbiting One of the Hottest and Brightest Known Exoplanet Host Stars

Brett C. Addison[1], Emil Knudstrup[2], Ian Wong[3,48], Guillaume Hébrard[4], Patrick Dorval[5], Ignas Snellen[5], Simon Albrecht[2], Aaron Bello-Arufe[6], Jose-Manuel Almenara[7], Isabelle Boisse[8], Xavier Bonfils[7], Shweta Dalal[4], Olivier D. S. Demangeon[9,10,11], Sergio Hoyer[8], Flavien Kiefer[12], N. C. Santos[9,11], Grzegorz Nowak[13,14], Rafael Luque[13,14], Monika Stangret[13,14], Enric Palle[13,14], René Tronsgaard[6], Victoria Antoci[2,6], Lars A. Buchhave[6], Maximilian N. Günther[15,49], Tansu Daylan[15,50], Felipe Murgas[13,14], Hannu Parviainen[13,14], Emma Esparza-Borges[13,14], Nicolas Crouzet[16], Norio Narita[13,17,18,19], Akihiko Fukui[13,17], Kiyoe Kawauchi[20], Noriharu Watanabe[19,21,22], Markus Rabus[23,24,25], Marshall C. Johnson[24], Gilles P. P. L. Otten[8,26], Geert Jan Talens[27], Samuel H. C. Cabot[28], Debra A. Fischer[28], Frank Grundahl[2], Mads Fredslund Andersen[2], Jens Jessen-Hansen[2], Pere Pallé[13,14], Avi Shporer[15], David R. Ciardi[29], Jake T. Clark[1], Robert A. Wittenmyer[1], Duncan J. Wright[1], Jonathan Horner[1], Karen A. Collins[30], Eric L. N. Jensen[31], John F. Kielkopf[32], Richard P. Schwarz[33], Gregor Srdoc[34], Mesut Yilmaz[35], Hakan Volkan Senavci[35], Brendan Diamond[36], Daniel Harbeck[24], Thaddeus D. Komacek[37,38], Jeffrey C. Smith[39,40], Songhu Wang[41], Jason D. Eastman[30], Keivan G. Stassun[42,43], David W. Latham[30], Roland Vanderspek[15], Sara Seager[3,15,44], Joshua N. Winn[45], Jon M. Jenkins[39], Dana R. Louie[37,46], Luke G. Bouma[45], Joseph D. Twicken[39,40], Alan M. Levine[15], and Brian McLean[47]

[1] University of Southern Queensland, Centre for Astrophysics, USQ Toowoomba, West Street, QLD 4350, Australia; Brett.Addison@usq.edu.au
[2] Stellar Astrophysics Centre, Department of Physics and Astronomy, Aarhus University, Ny Munkegade 120, DK-8000 Aarhus C, Denmark
[3] Department of Earth, Atmospheric, and Planetary Sciences, Massachusetts Institute of Technology, Cambridge, MA 02139, USA
[4] Institut d'Astrophysique de Paris, UMR7095 CNRS, Université Pierre & Marie Curie, 98bis boulevard Arago, F-75014 Paris, France
[5] Leiden Observatory, Leiden University, Postbus 9513, 2300 RA Leiden, The Netherlands
[6] DTU Space, National Space Institute, Technical University of Denmark, Elektrovej 328, DK-2800 Kgs. Lyngby, Denmark
[7] Université Grenoble Alpes, CNRS, IPAG, F-38000 Grenoble, France
[8] Aix Marseille Univ., CNRS, CNES, LAM, Marseille, France
[9] Instituto de Astrofísica e Ciências do Espaço, Universidade do Porto, CAUP, Rua das Estrelas, 4150-762 Porto, Portugal
[10] Centro de Astrofísica da Universidade do Porto, Rua das Estrelas, 4150-762 Porto, Portugal
[11] Departamento de Física e Astronomia, Faculdade de Ciências, Universidade do Porto, Rua Campo Alegre, 4169-007, Porto, Portugal
[12] LESIA, Observatoire de Paris, Université PSL, CNRS, Sorbonne Université, Université de Paris, 5 place Jules Janssen, F-92195 Meudon, France
[13] Instituto de Astrofísica de Canarias (IAC), E-38200 La Laguna, Tenerife, Spain
[14] Dept. Astrofísica, Universidad de La Laguna (ULL), E-38206 La Laguna, Tenerife, Spain
[15] MIT Kavli Institute for Astrophysics and Space Research, Massachusetts Institute of Technology, Cambridge, MA 02139, USA
[16] European Space Agency (ESA), European Space Research and Technology Centre (ESTEC), Keplerlaan 1, 2201 AZ Noordwijk, The Netherlands
[17] Komaba Institute for Science, The University of Tokyo, 3-8-1 Komaba, Meguro, Tokyo 153-8902, Japan
[18] JST, PRESTO, 3-8-1 Komaba, Meguro, Tokyo 153-8902, Japan
[19] Astrobiology Center, 2-21-1 Osawa, Mitaka, Tokyo 181-8588, Japan
[20] Department of Earth and Planetary Science, The University of Tokyo, Tokyo, Japan
[21] Department of Astronomical Science, The Graduate University for Advanced Studies, SOKENDAI, 2-21-1 Osawa, Mitaka, Tokyo 181-8588, Japan
[22] National Astronomical Observatory of Japan, NINS, 2-21-1 Osawa, Mitaka, Tokyo 181-8588, Japan
[23] Departamento de Matemática y Física Aplicadas, Universidad Católica de la Santísima Concepción, Alonso de Rivera 2850, Concepción, Chile
[24] Las Cumbres Observatory, 6740 Cortona Dr., Ste. 102, Goleta, CA 93117, USA
[25] Department of Physics, University of California, Santa Barbara, CA 93106-9530, USA
[26] Academia Sinica, Institute of Astronomy and Astrophysics, 11F Astronomy-Mathematics Building, NTU/AS campus, No. 1, Section 4, Roosevelt Rd., Taipei 10617, Taiwan
[27] Institut de Recherche sur les Exoplanètes, Département de Physique, Université de Montréal, Montréal, QC H3C 3J7, Canada
[28] Department of Astronomy, Yale University, 52 Hillhouse Ave, New Haven, CT 06511, USA
[29] NASA Exoplanet Science Institute, Caltech/IPAC, 1200 East California Avenue, Pasadena, CA 91125, USA
[30] Center for Astrophysics | Harvard & Smithsonian, 60 Garden Street, Cambridge, MA 02138, USA
[31] Department of Physics & Astronomy, Swarthmore College, Swarthmore, PA 19081, USA
[32] Department of Physics and Astronomy, University of Louisville, Louisville, KY 40292, USA
[33] Patashnick Voorheesville Observatory, Voorheesville, NY 12186, USA
[34] Kotizarovci Observatory, Sarsoni 90, 51216 Viskovo, Croatia
[35] Ankara University, Department of Astronomy and Space Sciences, TR-06100, Ankara, Turkey
[36] Howard Community College, 10901 Little Patuxent Pkwy, Columbia, MD 21044, USA
[37] Department of Astronomy, University of Maryland, College Park, MD 20742, USA
[38] Department of the Geophysical Sciences, The University of Chicago, Chicago, IL 60637, USA
[39] NASA Ames Research Center, Moffett Field, CA 94035, USA
[40] SETI Institute, 189 Bernardo Ave., Suite 200, Mountain View, CA 94043, USA
[41] Astronomy Department, Indiana University Bloomington, 727 East 3rd Street, Swain West 318, IN 47405, USA
[42] Department of Physics and Astronomy, Vanderbilt University, Nashville, TN 37235, USA
[43] Department of Physics, Fisk University, Nashville, TN 37208, USA
[44] Department of Aeronautics and Astronautics, Massachusetts Institute of Technology, 77 Massachusetts Avenue, Cambridge, MA 02139, USA

[45] Department of Astrophysical Sciences, Princeton University, Peyton Hall, 4 Ivy Lane, Princeton, NJ 08544, USA
[46] NASA Goddard Space Flight Center, 8800 Greenbelt Rd, Greenbelt, MD 20771, USA
[47] Space Telescope Science Institute, 3700 San Martin Drive, Baltimore, MD 21218, USA
Received 2021 April 11; revised 2021 August 11; accepted 2021 August 26; published 2021 December 6

Abstract

We present the discovery of a highly irradiated and moderately inflated ultrahot Jupiter, TOI-1431b/MASCARA-5 b (HD 201033b), first detected by NASA's Transiting Exoplanet Survey Satellite mission (TESS) and the Multi-site All-Sky Camera (MASCARA). The signal was established to be of planetary origin through radial velocity measurements obtained using SONG, SOPHIE, FIES, NRES, and EXPRES, which show a reflex motion of $K = 294.1 \pm 1.1\ \mathrm{m\,s^{-1}}$. A joint analysis of the TESS and ground-based photometry and radial velocity measurements reveals that TOI-1431b has a mass of $M_{\mathrm{p}} = 3.12 \pm 0.18\ M_{\mathrm{J}}$ ($990 \pm 60\ M_{\oplus}$), an inflated radius of $R_{\mathrm{p}} = 1.49 \pm 0.05\ R_{\mathrm{J}}$ ($16.7 \pm 0.6\ R_{\oplus}$), and an orbital period of $P = 2.650237 \pm 0.000003$ days. Analysis of the spectral energy distribution of the host star reveals that the planet orbits a bright ($V = 8.049$ mag) and young ($0.29^{+0.32}_{-0.19}$ Gyr) Am type star with $T_{\mathrm{eff}} = 7690^{+400}_{-250}$ K, resulting in a highly irradiated planet with an incident flux of $\langle F \rangle = 7.24^{+0.68}_{-0.64} \times 10^{9}\ \mathrm{erg\ s^{-1}\ cm^{-2}}$ ($5300^{+500}_{-470}\ S_{\oplus}$) and an equilibrium temperature of $T_{\mathrm{eq}} = 2370 \pm 70$ K. TESS photometry also reveals a secondary eclipse with a depth of 127^{+4}_{-5} ppm as well as the full phase curve of the planet's thermal emission in the red-optical. This has allowed us to measure the dayside and nightside temperature of its atmosphere as $T_{\mathrm{day}} = 3004 \pm 64$ K and $T_{\mathrm{night}} = 2583 \pm 63$ K, the second hottest measured nightside temperature. The planet's low day/night temperature contrast ($\sim$420 K) suggests very efficient heat transport between the dayside and nightside hemispheres. Given the host star brightness and estimated secondary eclipse depth of $\sim$1000 ppm in the K band, the secondary eclipse is potentially detectable at near-IR wavelengths with ground-based facilities, and the planet is ideal for intensive atmospheric characterization through transmission and emission spectroscopy from space missions such as the James Webb Space Telescope and the Atmospheric Remote-sensing Infrared Exoplanet Large-survey.

Unified Astronomy Thesaurus concepts: Exoplanets (498); Hot Jupiters (753); Transit photometry (1709); Radial velocity (1332)

Supporting material: data behind figures, machine-readable table

1. Introduction

Exoplanet discoveries over the past 25 years have revealed that the diversity of alien worlds to be far greater than we had ever imagined. Planets more massive than Jupiter were found on orbits measured in mere days (and became known as "hot Jupiters," e.g., Butler et al. 1998; Henry et al. 2000; Tinney et al. 2001), while others were found moving on highly eccentric orbits that had more in common with the solar system's cometary bodies than its planets (e.g., Naef et al. 2001; Jones et al. 2006; Wittenmyer et al. 2017, 2019; Bergmann et al. 2021). And more recently, a new class of close-in gas giants has emerged that are hotter than even the coolest main-sequence stars. These superhot gas giants are known as ultrahot Jupiters and have dayside temperatures $\gtrsim$2200 K (e.g., Parmentier et al. 2018).

In the early years of the exoplanet era, the majority of new exoplanet discoveries were made by radial velocity surveys (e.g., Mayor & Queloz 1995; Cochran et al. 1997; Butler et al. 1999; Pepe et al. 2004; Endl et al. 2008; Vogt et al. 2010) that mainly targeted stars considered to be "Sun-like": of spectral classes late-F, G, and K. The focus on such stars was, in part, driven by technical necessity—such stars possess ample spectral lines for radial velocity analysis and typically rotate slowly enough that such lines are sufficiently narrow to yield precise radial velocity measurements. As a result, during the first two decades of the exoplanet era, our knowledge of the diversity of planets was heavily biased toward systems with host stars similar to the Sun.

The situation changed with the launch of the Kepler space observatory, designed to search for exoplanets using the transit technique (Borucki et al. 2010). By surveying a vast number of stars at once, Kepler was able to get a true handle on the frequency of short-period planets around a wide variety of stars. It showed that planets are ubiquitous—a natural byproduct of the star formation process—and that planetary systems have a wide variety of architectures and compositions (e.g., Rogers 2015; Millholland et al. 2016, 2017; Guenther et al. 2017; Cañas et al. 2019; Dorn et al. 2019; Hsu et al. 2019; Bryson et al. 2021).

Although the transit technique is better suited to finding planets around hot, massive stars than the radial velocity method, such discoveries remain challenging due to the inherent difficulty in confirming planet candidates with radial velocity measurements. This is because more massive stars tend to have rapid rotation, resulting in a significant decrease in the obtainable radial velocity precision (e.g., WASP-167b/KELT-13b, KELT-17b, KELT-20b/MASCARA-2b, KELT-19Ab, HAT-P-69b, WASP-189b, HAT-P-70b, KELT-25b, KELT-26b, Zhou et al. 2016; Lund et al. 2017; Temple et al. 2017; Anderson et al. 2018; Talens et al. 2018; Siverd et al. 2018a; Zhou et al. 2019a; Martínez et al. 2020, transiting planets orbiting hot stars exclusively or primarily confirmed through Rossiter–McLaughlin or Doppler tomography observations).

NASA's Transiting Exoplanet Survey Satellite (TESS; Ricker et al. 2015) was launched in 2018 and is the successor to the hugely successful Kepler and K2 missions. While the Kepler spacecraft could only examine a $\sim$115° patch of sky ($\sim$0.3% of the total area of the full sky) at any given time (performing a narrow but deep survey of the sky), TESS is

[48] Pegasi b Fellow.
[49] Juan Carlos Torres Fellow.
[50] Kavli Fellow.

designed to survey large bands of the sky at a time (96° by 24°). As a result, over the two years of TESS' primary mission, it surveyed the majority of the sky, obtaining high-cadence observations (one target pixel image recorded every two minutes) of more than 200,000 pre-selected main-sequence dwarf stars, and low-cadence observations (one full frame image every 30 minutes) of 20 million bright stars (Ricker et al. 2015). In doing so, it has enabled the search for planets around a wide variety of bright stars (including hot and more massive stars historically avoided in radial velocity surveys)—perfect targets for ground-based follow-up observations. While we are still in the early stages of reaping the full harvest from TESS' remarkable wealth of observations, the spacecraft has already discovered a variety of new exoplanet systems (e.g., Huang et al. 2018; Cañas et al. 2019; Günther et al. 2019; Jones et al. 2019; Newton et al. 2019; Wang et al. 2019; Addison et al. 2021; Brahm et al. 2020; Davis et al. 2020; Gilbert et al. 2020; Jordán et al. 2020; Plavchan et al. 2020; Rodriguez et al. 2020; Teske et al. 2020) with many planet candidates, or TESS Objects of Interests (TOIs), awaiting confirmation (Guerrero et al. 2021).

A great benefit of TESS' discoveries orbiting bright stars is that those stars make ideal targets for follow-up observations, allowing us to better characterize the planets that orbit them. The most obvious route by which such characterization is achieved is through radial velocity observations, which provide measurements of the masses of the planets. Additionally, radial velocity observations also provide vital information on the planet's orbit, including its eccentricity and orbital period (critical if only one or two transits are observed). These observations can also be used to reveal the presence of otherwise undetectable, nontransiting planetary companions (e.g., Mills et al. 2019; Weiss et al. 2020; Sozzetti et al. 2021). When radial velocity observations are made during a transit of a planet across the disk of its host star, they can be used to constrain the inclination of the planet's orbit relative to the plane of the host star's equator through the use of the "Rossiter–McLaughlin effect" (e.g., McLaughlin 1924; Rossiter 1924).

Such observations have yielded startling insights in recent years. Where predictions made based on our knowledge of the solar system would suggest that exoplanets should typically move in roughly the same plane as their host star's equator, Rossiter–McLaughlin observations have revealed that a significant fraction of hot Jupiters move on misaligned orbits. Surprisingly, such observations have even revealed a number of planets moving on polar or retrograde orbits (e.g., Narita et al. 2009; Winn et al. 2009; Hirano et al. 2011; Albrecht et al. 2012; Addison et al. 2013)—a scenario markedly different from the near coplanarity of the solar system (as discussed in Horner et al. 2020 and references therein).

The highly excited orbits of such inclined hot Jupiters are likely linked to their origins. A number of different mechanisms have been proposed to produce hot Jupiters, ranging from the smooth and relatively sedate inward migration of the giant planets through interactions with their host star's protoplanetary disk (e.g., Lin et al. 1996; Ward 1997; Tanaka et al. 2002; Alibert et al. 2005), to planet–planet scattering (where close encounters between two planets throw them both onto highly eccentric orbits, dropping one inwards, toward its host, and flinging the other outwards; see, e.g., Chatterjee et al. 2008; Beaugé & Nesvorný 2012; Li et al. 2019a), and even distant perturbations from binary companions (through the Kozai–Lidov mechanism; see, e.g., Kozai 1962; Lidov 1962; Nagasawa et al. 2008). Those mechanisms that invoke a period of high orbital eccentricity then require the tidal circularization of the planet's orbit, which, for small pericenter distances, can happen on timescales far shorter than the lifetimes of the stars involved (Nagasawa et al. 2008).

These three methods would naturally produce very different populations of hot Jupiters. Those formed through disk migration would be expected to orbit in essentially the same plane as their host star's equator. Those formed through planet–planet scattering would likely also congregate around such low inclinations, but would be more dispersed/excited, with scattering events able to produce at least moderate orbital inclinations for the planets involved. Planets that migrate as a result of the Kozai–Lidov mechanism, by contrast, would be expected to be found on highly misaligned orbits, because the Kozai–Lidov mechanism causes significant inclination excitation as a byproduct of the eccentricity excitation driving the planetary migration.

Given that more massive stars are statistically more likely to host binary companions (e.g., Perryman et al. 1998; Böhm-Vitense 2007; Zinnecker & Yorke 2007), especially Am stars such as TOI-1431 (see Böhm-Vitense 2006), and also tend to form more massive planets (e.g., Ida & Lin 2005; Bowler et al. 2010; Reffert et al. 2015), it would seem reasonable to expect that such stars might be more likely to host both moderately and highly misaligned planets (since the two mechanisms by which excited hot Jupiters can be produced would be more likely to occur). Indeed, as the catalog of planets for which spin–orbit alignment measurements have been made has grown, this prediction appears to have been borne out. The fraction of highly misaligned planets appears to be a strong function of stellar effective temperature (and to a lesser degree stellar mass), with hotter and more massive stars far more likely to host such planets than those that are cooler and less massive (e.g., Triaud et al. 2010; Winn et al. 2010; Louden et al. 2021).

In this work, we expand the catalog of planets orbiting hot main-sequence stars with the discovery and characterization of TOI-1431 b/MASCARA-5b—an inflated, ultrahot Jupiter orbiting a massive, hot, and metal-peculiar Am star.

In Section 2, we describe the observations and data reduction. The host star properties derived from the analysis of the broadband spectral energy distribution (SED) and spectroscopy are outlined in Section 3. The data analysis, modeling, and results are presented in Section 4. We then discuss the phase curve and secondary eclipse analysis and measurements of the planet's dayside and nightside temperatures in Section 4.1. Lastly, the discussion and conclusions are provided in Sections 5 and 6, respectively.

2. Observations and Data Reduction

TOI-1431/MASCARA-5 (HD 201033) was observed with space-based photometry by TESS (Section 2.1) and ground-based photometry from several facilities (Section 2.2). We also obtained follow-up spectroscopic observations from several ground-based facilities (Section 2.3) as well as high-contrast imaging on the Keck II telescope (Section 2.4) to establish the planetary nature of the transit signals detected by TESS and the Multi-site All-Sky Camera (MASCARA). Here we describe the observations collected and the data reduction process.

2.1. TESS Photometry

The star TOI-1431 (HD 201033; TIC 375506058, Stassun et al. 2019) was observed in Sectors 15 (on Camera 2 and CCD chip number 4) and 16 (on Camera 2 and CCD chip number 3) by TESS in 2 minute cadence mode nearly continuously between 2019 August 15 and 2019 October 7. The photometric data were processed by the TESS Science Processing Operations Center (SPOC) pipeline (see Jenkins et al. 2016 for a description of the SPOC pipeline), resulting in two versions of the light curves: simple aperture photometry (SAP, see Twicken et al. 2010; Morris et al. 2020) and multiscale maximum a posteriori (MAP) presearch data conditioning (PDC, see Smith et al. 2012; Stumpe et al. 2012, 2014). Multiscale MAP PDC divides each light curve into three wavelet bandpasses and then performs a MAP-like correction in each using separate cotrending basis vectors derived within each bandpass. A fit to neighboring targets is used as the Bayesian prior during the a posteriori fit. We downloaded both versions of the light curves from NASA's Mikulski Archive for Space Telescopes (MAST). Additionally, we produced a third version of the TESS light curve, single-scale MAP PDC (where no band-splitting is performed, Smith et al. 2012), for the analysis described in Section 4.

The transiting planet candidate was promoted to TOI status (see TOI catalog, Guerrero et al. 2021) and designated TOI-1431.01 by the TESS Science Office based on model fit results and a passing grade on all diagnostic tests in the SPOC Data Validation (DV) report (Twicken et al. 2018; Li et al. 2019b) for Sector 15. Twenty transits (10 per sector) were observed by TESS. Each transit had a duration of ∼2.5 hr, a depth of ∼6000 parts per million (ppm), and recurred with a period of 2.65 days. The first detected transit occurred on $\mathrm{BJD_{TDB}}$ 2,458,712 in Sector 15. The raw SAP and multiscale MAP PDC light curves are shown in Figure 1.

Before detrending and fitting the SAP and the two versions of the PDC light curves, we first removed all quality-flagged data. The light curves were then split into a total of 10 segments, with each segment split at the spacecraft momentum dumps[51] at intervals of 4.25 and 5.83 days in Sectors 15 and 16, respectively, to minimize the offset effects on the light curves during the detrending and fitting analysis. The transits were then masked and a 5σ median filter was applied to the out-of-transit data to remove remaining outliers in each light-curve segment. Lastly, the light-curve segments were normalized with the mean of the out-of-transit flux before performing the detrending and fitting analysis as described in Section 4.

2.2. Ground-based Transit Photometry

Transit signals of TOI-1431b were first detected by the ground-based MASCARA telescope (Talens et al. 2017) at the Roque de los Muchachos Observatory, La Palma, starting 2015 February. Transits were observed by MASCARA between 2015 February and 2018 March and were discovered before TESS observed them. Figure 2 shows the phase-folded light curve of TOI-1431b from MASCARA with the transit signal clearly detected at the same period of ∼2.65 days and approximate transit depth as measured by TESS. The MASCARA observations were taken with exposure times of 6.4 s without using any filters and achieved a photometric precision of ∼5000 ppm per 5 m binned observation.

Both MASCARA and TESS have large on-sky pixel sizes of $1'\,\mathrm{pixel}^{-1}$ (Talens et al. 2017) and $0\farcs35\,\mathrm{pixel}^{-1}$ (Ricker et al. 2015), respectively. As such, further photometric follow-up is required to rule out potential false positive scenarios such as nearby eclipsing binaries, where an eclipsing binary pair falls on or very close to the same pixel as the target star in the MASCARA and TESS images.

To confirm the transit signals detected by TESS and MASCARA were coming from TOI-1431 and to check for any changes in transit depth between multiple photometric bands (chromaticity), we acquired additional photometric follow-up observations from several ground-based facilities through the TESS Follow-up Observing Program Working Group as summarized in Table 3 in the Appendix. We used the TESS Transit Finder, which is a customized version of the Tapir software package (Jensen 2013), to schedule the observations. These facilities include the 0.36 m CDK14 telescope at Howard Community College, the MuSCAT2 imager on the 1.52 m Carlos Sanchez Telescope (TCS) at the Teide Observatory (OT), the 0.8 m telescope at the Ankara University Kreiken Observatory (AUKR), the 0.3 m telescope at the Kotizarovci Observatory (SCT) in Rijeka, Croatia, the 0.6 m University of Louisville Manner Telescope (ULMT) at Mt Lemmon, and the Las Cumbres Observatory Global Telescope (LCOGT; Brown et al. 2013) 1 m node at the McDonald Observatory. For the final global analysis with `Allesfitter`, we included only the high-quality and high-precision (rms $\lesssim$3 ppt) ground-based observations with full transit coverage that are free of significant systematics to provide precise transit depth measurements and accurate transit ephemeris. As such, we have not included the light curve taken on 2020 May 24 from MuSCAT2 (but we do include the 2020 May 16 observation) due to significant systematics (see Section 2.2.2), ULMT taken on 2020 September 28 due to systematics and moderately low precision photometry obtained (∼3.4 ppt), nor the photometry from MASCARA due to its relatively low photometric precision of ∼5 ppt.

2.2.1. CDK14

One full transit of TOI-1431b was observed on 2019 December 24–25 with the CDK14 telescope at Howard Community College. The observations were taken using alternating 10 s exposures in the Sloan g' and z_s filters, starting at 23:02 UT on December 24 at an airmass of 1.2 and finishing at 02:56 UT on December 25 at an airmass of 2.4. We reduced the data and extracted the light curves for each filter using the `AstroImageJ` (`AIJ`) software package (Collins et al. 2017) with 7 pixel apertures. Figure 3 shows the transit signatures in the two bands with fitted transit depths of $5.1^{+0.6}_{-0.7}$ ppt and $5.1^{+0.5}_{-0.6}$ ppt for the Sloan g' and z_s filters, respectively. These transit depths are consistent with the SPOC pipeline transit depth of 5.68 ± 0.03 ppt to within $\sim 1\sigma$.

2.2.2. MuSCAT2

Two full transits of TOI-1431b were observed with MuSCAT2, one on 2020 May 16 and a second one on 2020 May 24, using simultaneous multicolor photometry in g', r', i', and z_s bands (Narita et al. 2019). For the joint fitting, we only used the transit observed on 2020 May 16 since the second

[51] As provided in the data release notes found at https://archive.stsci.edu/tess/tess_drn.html.

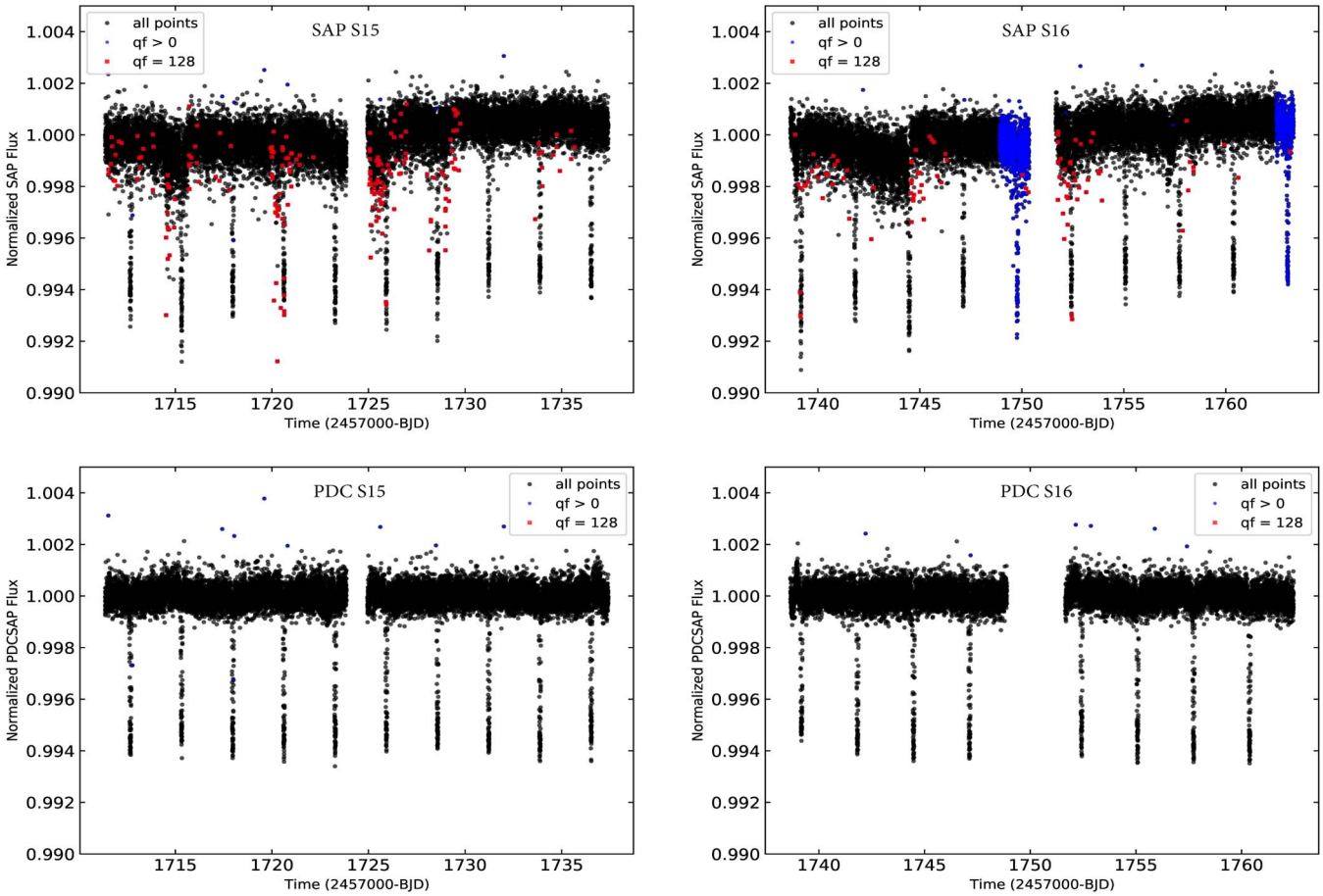

Figure 1. The TESS light curves of TOI-1431 from Sectors 15 (left) and 16 (right). The top panels show the simple aperture photometry and the bottom panels show the presearch data conditioning versions of the light curves. The circles plotted in blue represent data that have a quality flag greater than 0 (but not equal to 128) and the red squares are data with quality flag equal to 128 (flagged as manual exclude, i.e., the cadence was excluded because of an anomaly). The TESS quality flags are described in the TESS Data Products Description Document (see https://archive.stsci.edu/missions/tess/doc/EXP-TESS-ARC-ICD-TM-0014-Rev-F.pdf.

transit observation was affected by systematics due to weather, resulting in different transit depths between the filter bands and residuals larger than 1.0 ppt. On the night of 2020 May 16, defocused observations were taken from 01:50 UT to 05:22 UT, with exposure times of 8 s for all channels, except for the r', where an exposure time of 5 s was used for autoguiding. We reduced the data and extracted the light curves using the standard MuSCAT2 pipeline (Parviainen et al. 2019), recovering the expected transit signal as shown in Figure 3. Figure 14 in the Appendix shows the transit light curve in all four bands with fits to the transits and systematics, fits to the transits with systematics removed, and the resulting residuals.

2.2.3. AUKR

A full transit of TOI-1431b was observed with the 0.8 m Prof. Dr. Berahitdin Albayrak Telescope (T80) at the AUKR on 2020 June 16 in the Sloan z_s band. Observations started approximately 30 minutes before transit ingress at 21:15 UT and lasted until 01:13 UT the following day, with exposure times of 40 s, and the target was observed at an airmass between 1.0 and 1.3. We extracted the photometry using the `AIJ` software package with 12 pixel (8.″16) apertures, and the resulting fit to the light curve is shown in Figure 4. The measured transit depth of $4.5^{+0.5}_{-0.6}$ ppt is moderately shallower than the transit depths found from the TESS and other ground-based light curves, likely due to unaccounted for systematics.

2.2.4. SCT

We used the 0.3 m telescope at the Kotizarovci Observatory near Viskovo, Croatia, to observe a full transit of TOI-1431b on 2020 August 8. The transit was observed in the TESS-like band with 20 s exposures continuously for nearly 6.5 hr starting at 20:23 UT and ending at 02:45 UT in low airmass that ranged from 1.″1 at the start to 1.″3 at the end of the observations. The photometry was processed using the `AIJ` software package with an aperture of 11 pixels (13.″2) and Figure 4 shows the resulting fit to the light curve. We measure a transit depth of $5.6^{+0.2}_{-0.3}$ ppt, consistent with the depth measured from the TESS light curves.

2.2.5. ULMT

On 2020 September 20, we observed a full transit of TOI-1431b from the 0.6 m ULMT at Mt Lemmon using the Sloan z' filter. We set the exposure length to 32 s and started the observations at 04:29 UT. The observing was interrupted between 06:57 UT and 07:31 UT, around the start of transit ingress, due to a guiding error and then resumed afterwards until 10:26 UT. The target was observed at an airmass of 1.1 at the start and airmass of 1.8 at the end of the observations. The images were bias- and dark-corrected and the light curve was extracted using an aperture of 13 pixels (5.″1) with the `AIJ` software package. We measure a transit depth of 5.8 ± 0.3 ppt

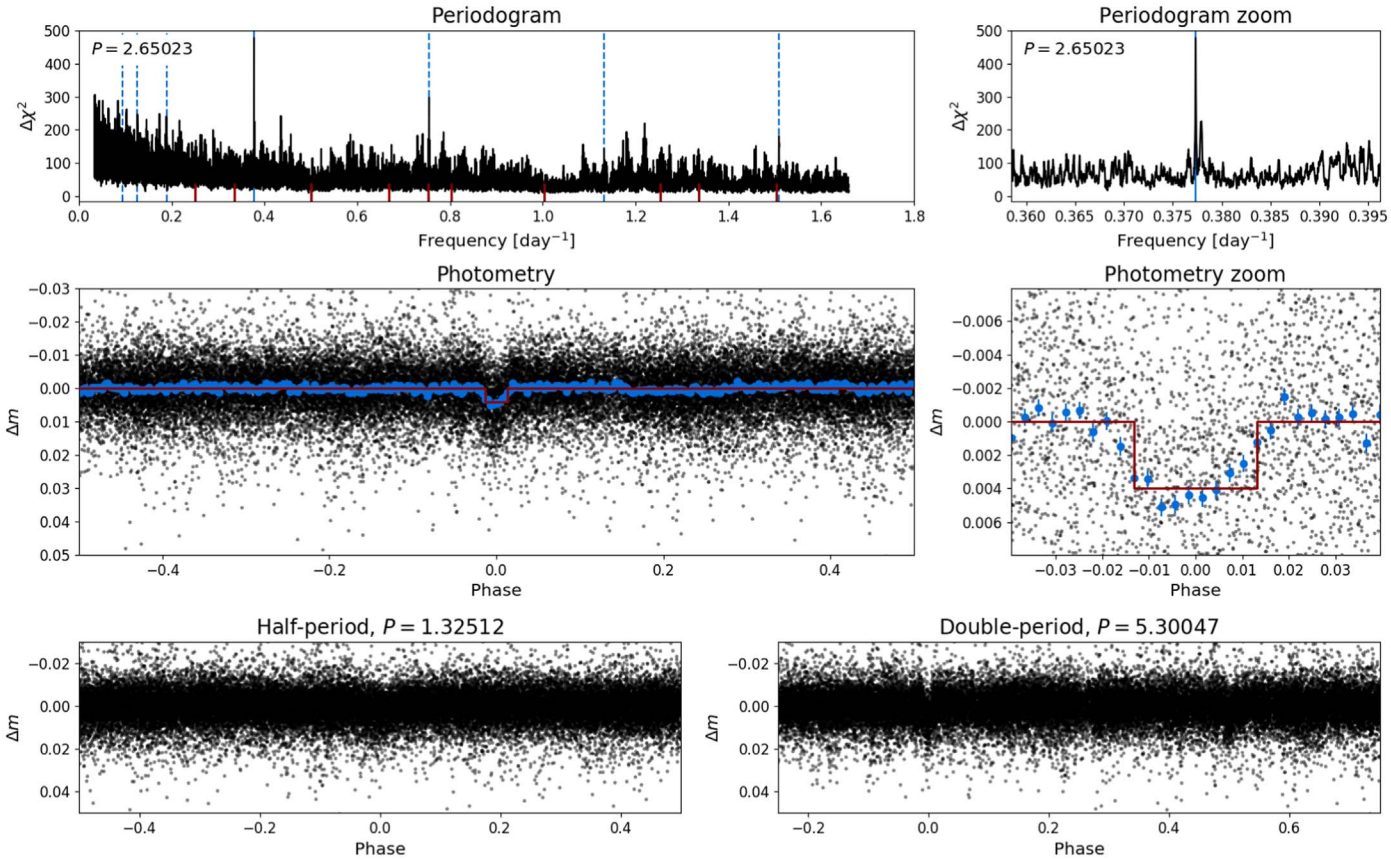

Figure 2. Photometry of TOI-1431 taken from the Multi-site All-Sky Camera (MASCARA) telescope at the Roque de los Muchachos Observatory, La Palma. The top panels are the box least-squares periodograms from the MASCARA light curves showing the strongest peak period at 2.65023 days. The middle panels show the phase-folded light curve from MASCARA, full phase on the left and zoomed in on the transit on the right. The blue points represent binned data in 0.003 phase steps, the black points are the original observations in bins of 50 images (320 s), and the red line is the best-fit box least-squares model (see Kovács et al. 2002) used in detecting the transit. The bottom panels show the photometry phase-folded at half and double the period (bottom left and right, respectively) found at the strongest peak in the periodogram. No obvious dip features are seen in the half-period phase-folded plot but two dip features are apparent in the double-period phase-folded plot at phase 0 and 0.5, as expected for the transiting planet with a period of 2.65023 days. The MASCARA light curves were not used in the global modeling in `Allesfitter`.

(see Figure 4), in excellent agreement with the depth measured from the TESS photometry.

2.2.6. LCOGT

A full transit of TOI-1431b was observed on 2020 October 14 from the LCOGT 1.0 m network node at McDonald Observatory near Fort Davis, Texas (LCO-McD), in PAN-STARRS Y band. The SINISTRO camera images were calibrated using the standard LCOGT `BANZAI` pipeline (McCully et al. 2018), and the photometry was extracted using the `AIJ` software package with 20 pixel (7″.8) apertures. Figure 4 shows a clear transit detection with an individually fitted transit depth of 5.7 ± 0.3 ppt, consistent with the SPOC pipeline transit depth of 5.68 ± 0.03 ppt to within 1σ.

2.3. Spectroscopic Observations

We obtained high-resolution (HR) spectroscopic observations of TOI-1431 with SONG, SOPHIE, FIES, NRES (TLV and ELP), and EXPRES to establish the planetary nature of the TESS transiting candidate and measure its mass. Here we describe the observations from each spectrograph and list the derived radial velocities (RVs) in Table 4 in the Appendix.

2.3.1. SONG

High-resolution spectroscopic observations of TOI-1431 were obtained using the robotic Stellar Observations Network Group (SONG) 1 m Hertzsprung telescope at the Teide Observatory in Tenerife (Andersen et al. 2014; Fredslund Andersen et al. 2019). In total, 19 spectra were taken with SONG between 2020 March 6 and 2020 June 29. SONG is equipped with an HR coudé echelle spectrograph with wavelength coverage between 4400 and 6900 Å across 51 spectral orders. The observations were taken using the iodine cell to allow for precise wavelength calibration. For each observation, we took a 2400 s exposure in slit mode 6 (slit width 1″.2), providing a spectral resolution of $R = 90{,}000$, a median count per pixel at 5560 Å of 1795.2 ADU (signal-to-noise ratio (S/N) of at least 50 per resolution element for all observations), and median radial velocity precision of 29 m s^{-1}.

Before each target observation, calibration frames (including bias frames, flat fields, and ThAr spectra) were taken on the same night and applied to target images. The target observations were then reduced and the spectra extracted with a pipeline written in Python. This pipeline uses a C++ implementation of the optimal extraction method from Ritter et al. (2014). We also acquired observations of the bright fast-rotating star HR 5191 that was used as an intrinsic stellar template for determining the spectral-line-spread function of

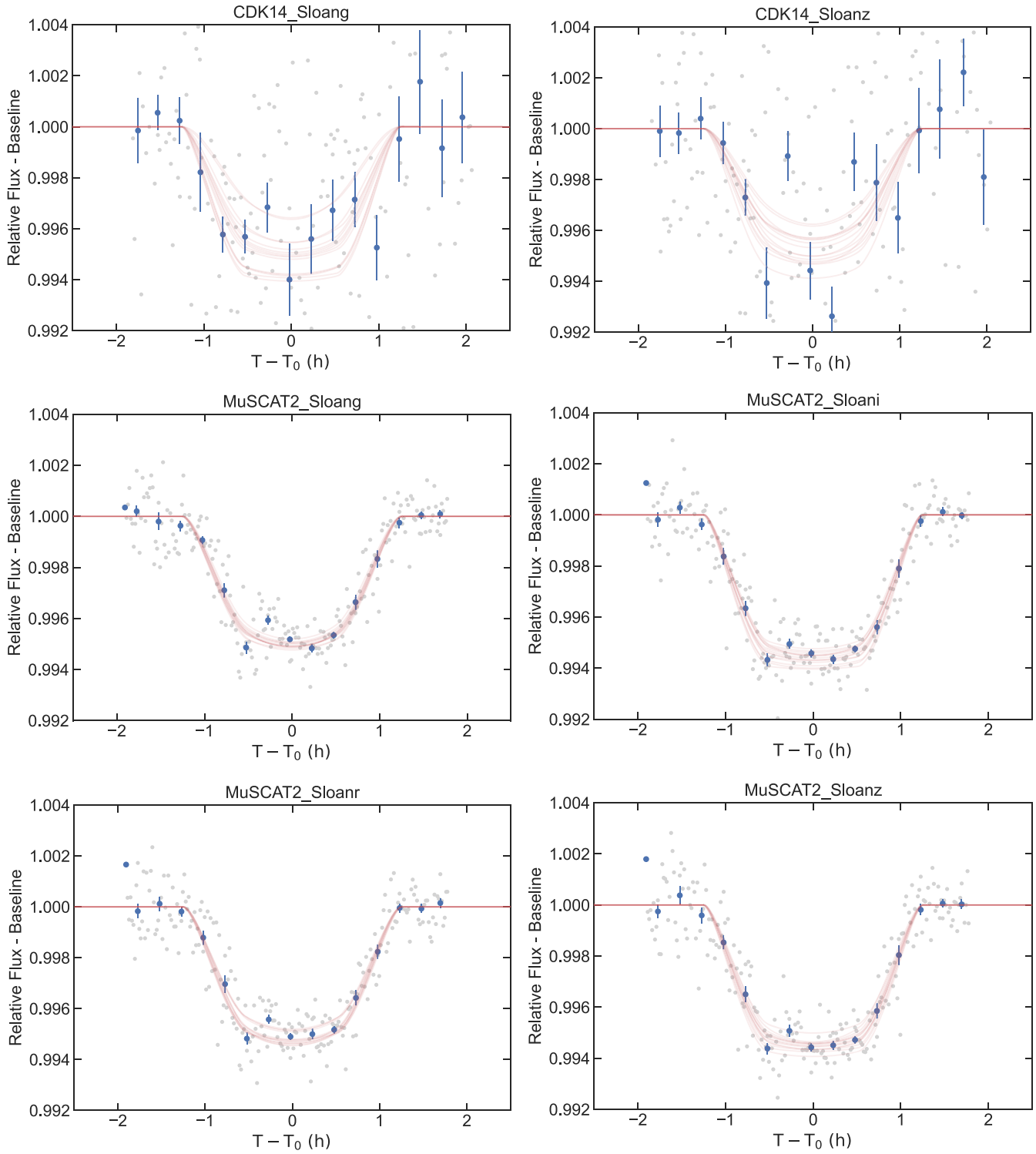

Figure 3. The ground-based transit light curves of TOI-1431b/MASCARA-5 b as a function of time from the observations taken with the two CDK14 photometric bands and the four MuSCAT2 photometric bands. The normalized photometric measurements are represented by the gray points while the blue points are the binned photometry. The 15 red lines are the randomly drawn transit light-curve models from the nested sampling posterior.

(The data used to create this figure are available.)

the spectrograph and to deconvolve a high S/N spectrum of TOI-1431 taken without the iodine cell. We then analyzed the extracted spectra using the iSONG pipeline (Antoci et al. 2013) to produce radial velocities (given in Table 4 and shown in Figure 5), following the procedure of Grundahl et al. (2017).

2.3.2. *SOPHIE*

TOI-1431 was observed with the fiber-fed SOPHIE HR echelle spectrograph on the 1.93 m telescope at the Haute-Provence Observatory (Perruchot et al. 2008, 2011) between 2019 December 18 and 2020 January 12. We collected a total

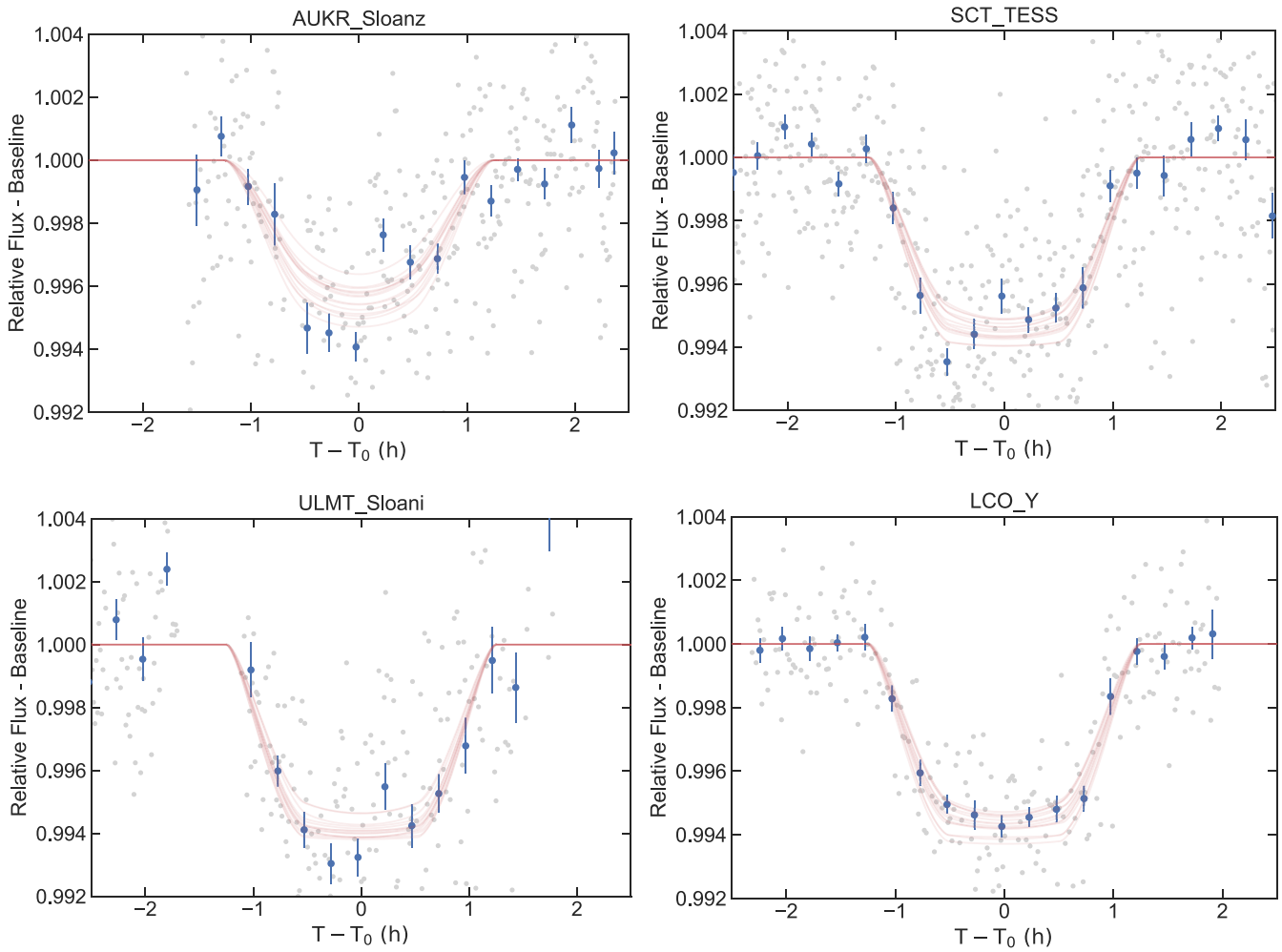

Figure 4. Same as Figure 3, but showing the observations taken with AUKR, SCT, ULMT, and LCO.
(The data used to create this figure are available.)

of eight spectra in the HR mode ($R = 75{,}000$ at 5500 Å). The second SOPHIE aperture allowed us to check that there was no background sky pollution.

Thorium–argon calibration spectra were taken at the start of each night of the observations to determine the wavelength calibration zero-point, as well as Fabry–Perot étalon spectra regularly during the nights to monitor any possible instrumental drift. The spectra cover the wavelength range from 3872 to 6943 Å across 41 spectral orders, of which 39 were extracted and used for computing the radial velocities. The exposure times ranged from 214 to 490 s, resulting in a uniform S/N for each observation of 50 per resolution element at 5500 Å and median Doppler velocity precision of 7 m s^{-1}.

The spectroscopic data were reduced and then extracted using the standard SOPHIE pipeline (Bouchy et al. 2009), which performs optimal order extraction, cosmic-ray rejection, and wavelength calibration. Radial velocities were computed using the cross-correlation technique and a numerical binary mask corresponding to a star of F0 spectral type (e.g., see Courcol et al. 2015), the closest available binary mask to TOI-1431's spectral type. Table 4 list the radial velocities from SOPHIE and they are shown in Figure 5. The width of the cross-correlation function (CCF) allows us to measure the rotational velocity of the star as $v \sin i = 6.0 \pm 0.2$ km s^{-1}.

2.3.3. FIES

We acquired 52 spectra of TOI-1431 using the Fibre-fed Echelle Spectrograph (FIES; Frandsen & Lindberg 1999; Telting et al. 2014) at the 2.56 m Nordic Optical Telescope (NOT; Djupvik & Andersen 2010) of Roque de los Muchachos Observatory (La Palma, Spain). The observations were carried out between 2019 November 27 and 2020 June 20 (UT). We used the FIES HR mode, which provides a resolving power of $R = 67{,}000$ in the spectral range 3760–8220 Å. We traced the RV drift of the instrument by acquiring long-exposure ThAr spectra ($T_{\rm exp} \approx 90$ s) immediately before and after each science exposure. The exposure time was set to 300–900 s, depending on the sky conditions and scheduling constraints.

The data reduction follows the steps of Buchhave et al. (2010) and includes optimal extraction of the spectrum and interpolation of the ThAr wavelength solutions. The S/N per resolution element at 5500 Å of the extracted spectra is in the range 42–127. We cross-correlate each observation order-by-order in velocity space against the strongest exposure of the star (BJD = 2,458,995.703476). Finally, the radial velocity of each observation is measured from the peak of the summed CCF and transformed to the barycentric frame. The uncertainties for the

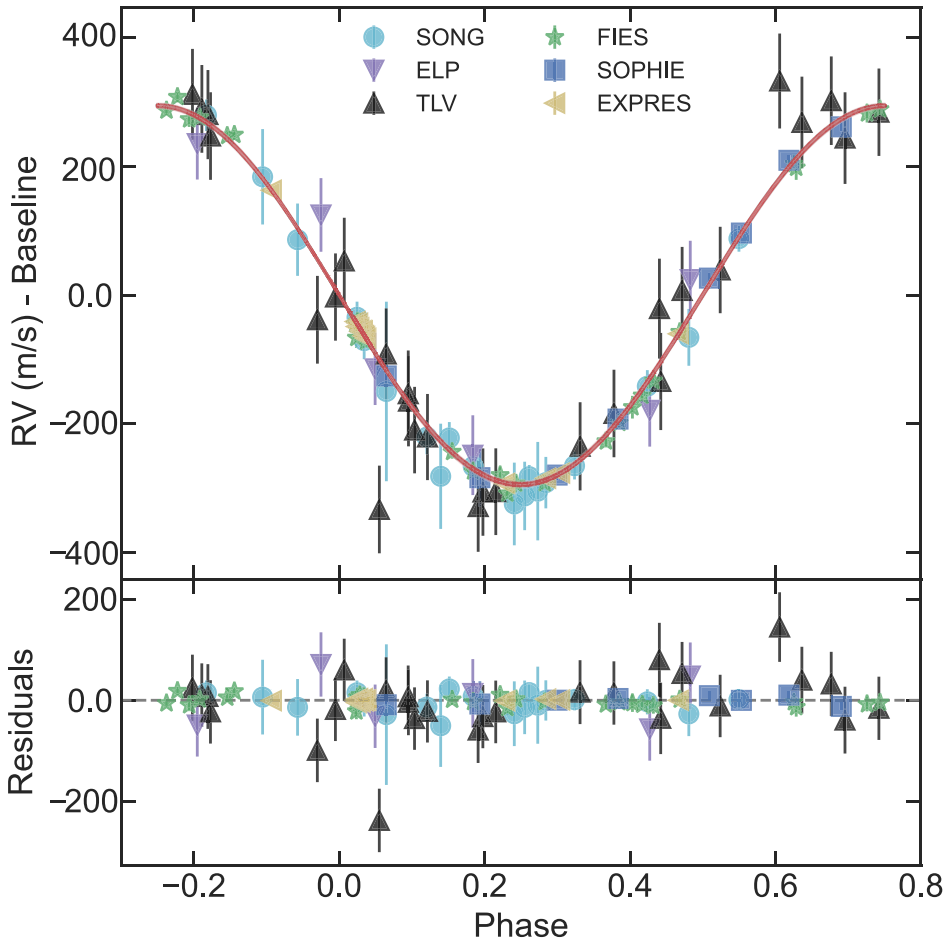

Figure 5. Radial velocity measurements of TOI-1431b/MASCARA-5 b as a function of orbital phase. The radial velocities from SONG, NRES (ELP and TLV), FIES, SOPHIE, and EXPRES are represented by the cyan colored circles, purple triangles pointed down, black triangles pointed up, green stars, blue squares, and gold triangles pointed to the left, respectively. A random selection of 20 radial velocity curves drawn from the posterior of the nested sample modeling are plotted as the red lines. The bottom panel shows the residuals between the data and the best-fit (posterior median) model.

derived radial velocities are 7.2–19.1 $\mathrm{m\,s^{-1}}$ with a mean value of 12.2 $\mathrm{m\,s^{-1}}$.

2.3.4. NRES

We triggered observations of TOI-1431 on the Network of Robotic Echelle Spectrographs (NRES) (Siverd et al. 2018b), operated by the LCOGT (Brown et al. 2013). NRES consists of four similar spectrographs with two in the Northern Hemisphere and two in the Southern. The spectrographs cover the wavelength range from 380 to 860 nm with a resolution of $R \sim$ 53,000. They are fiber-fed, where one fiber observes the science target and the second fiber is used for the wavelength calibration source. In the case of NRES the calibration source is a ThAr lamp.

Due to the target's Northern declination, TOI-1431 was accessible and observed by the units at the Wise Observatory (TLV) and the McDonald Observatory (ELP). We obtained a total of 34 spectra. For spectral classification we used the standard NRES pipeline in combination with SpecMatch-Synth code.[52] In order to obtain high-precision RV measurements, we processed the spectra using an adapted version of the CERES pipeline (Brahm et al. 2017).

[52] https://github.com/petigura/specmatch-syn

2.3.5. EXPRES

We observed TOI-1431 with the Extreme Precision Spectrometer (EXPRES) (Jurgenson et al. 2016), which was recently commissioned at the 4.3 m Lowell Discovery Telescope (Levine et al. 2012). EXPRES is a vacuum-stabilized and fiber-fed optical spectrograph, operating between 380 and 780 nm at a resolution of $R \sim$ 137,500. It achieves a single-measurement radial velocity precision of approximately 30 cm $\mathrm{s^{-1}}$ at S/N of 250 per pixel (Petersburg et al. 2020). The wavelength solution is determined from both a ThAr lamp and a Menlo Systems laser frequency comb. Recent performance benchmarks and science results are shown by Blackman et al. (2020) and Brewer et al. (2020), and the radial velocity pipeline is discussed by Petersburg et al. (2020). For TOI-1431, we acquired 15 observations with EXPRES and achieved a mean radial velocity precision of 2.1 $\mathrm{m\,s^{-1}}$.

2.4. High-contrast Imaging Observations

We obtained high-angular-resolution imaging of TOI-1431 using the NIRC2 instrument on the Keck II. The observations were taken on the night of 2020 September 9 UTC under clear skies, very good seeing conditions of $\sim 0\farcs4$, and at an airmass of 1.25. The resulting 5σ detection sensitivity and adaptive optics (AO) image from the NIRC2 observations are plotted in

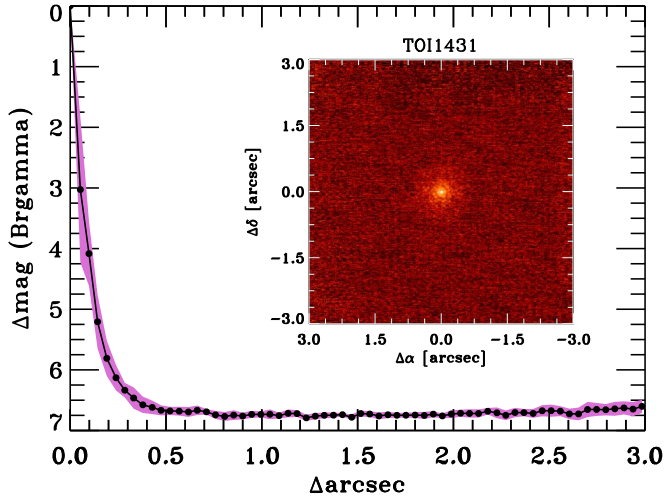

Figure 6. The 5σ detection sensitivity and AO image from Keck II NIRC2 high-angular-resolution imaging of TOI-1431 in the Brγ band. The orientation of the AO image has north pointed up and east to the left. No stars were detected within 3″ of TOI-1431.

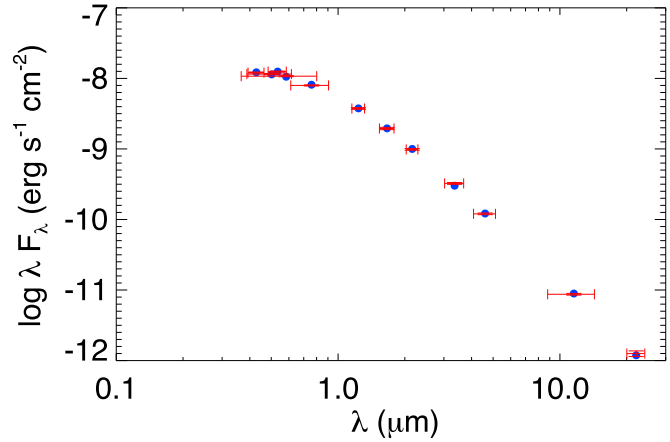

Figure 7. The SED for TOI-1431. The red symbols are the broadband photometric measurements used in the SED analysis (provided in Table 1) with the horizontal uncertainty bars representing the effective width of the passband. The blue symbols are the model fluxes from the best-fit Kurucz atmosphere model.

Figure 6. No nearby companions or background sources were detected within 3″ of TOI-1431.

3. Host Star Properties

TOI-1431/MASCARA-5 (HD 201033) is a bright ($V = 8.049$) Am (chemically peculiar, kA5mF2) type star (Figueras et al. 1991; Renson et al. 1991; Renson & Manfroid 2009) with a Gaia DR2 parallax of 6.686 ± 0.046 mas (Gaia Collaboration et al. 2018) and distance of $149.6^{+1.1}_{-1.0}$ pc. The star has a radius of $1.92 \pm 0.07\,R_\odot$, mass of $1.90^{+0.10}_{-0.08}\,M_\odot$, surface gravity of $\log g = 4.15 \pm 0.04$ dex, effective temperature of 7690^{+400}_{-250} K, metallicity of $[\mathrm{Fe/H}] = 0.43^{+0.20}_{-0.28}$ dex, and luminosity of $11.7^{+2.3}_{-1.2}\,L_\odot$, derived from an analysis of the broadband SED and the Yonsei Yale (YY) stellar evolutionary models (Yi et al. 2001) using EXOFASTv2 (Eastman et al. 2019) as discussed in Section 3.1. We also derive independent values for the effective temperature and metallicity from the analysis of SONG, SOPHIE, and FIES spectra in Section 3.2.

3.1. SED Analysis

We performed a SED analysis of TOI-1431 using EXOFASTv2 to derive stellar parameters independent of those from spectroscopy. We used broadband photometry obtained from the Tycho (Høg et al. 2000), Two Micron All Sky Survey (2MASS, Cutri et al. 2003), WISE (Cutri et al. 2013), and Gaia (Gaia Collaboration et al. 2018) catalogs for the fitting of the SED (Figure 7). Gaussian priors were placed on the parallax from Gaia DR2, adding 82 μas to correct for the systematic offset found by Stassun & Torres (2018) and adding the 33 μas uncertainty in their offset in quadrature to the Gaia-reported uncertainty. We applied an upper limit on the V-band extinction of 3.4905 from the Schlafly & Finkbeiner (2011) dust maps at the location of TOI-1431 as well as an upper limit on the dilution effects of nearby stars of 0.00484 as reported in the TESS SPOC light curve file. The SED analysis ran until convergence, i.e., the Gelman–Rubin statistic (R_z) and the number of independent chain draws (T_z) were less than 1.01 and greater than 1000, respectively (see Eastman et al. 2019). The YY stellar evolutionary models were used instead of the default MESA isochrones and stellar tracks (MIST) to determine the stellar radius ($R_\star$), mass ($M_\star$), effective temperature ($T_{\rm eff}$), luminosity ($L_\star$), metallicity ([Fe/H]), surface gravity ($\log g$), and age of TOI-1431, which are given in Table 1. We found that using the MIST models resulted in many of the Markov Chain Monte Carlo (MCMC) steps reaching the [Fe/H] grid's upper limit of 0.5 dex while the MCMC chains never reached the [Fe/H] upper limit of 0.78 dex using the YY tracks. The YY evolutionary models are better suited for hot metal-rich stars such as TOI-1431.

From the best-fit Kurucz stellar atmosphere model from the SED and the best-fitting YY stellar evolutionary model (Figure 8), we find that TOI-1431 is a very hot and metal-rich A-type star with $R_\star = 1.92 \pm 0.07\ R_\odot$, $M_\star = 1.90^{+0.10}_{-0.08}\ M_\odot$, $T_{\rm eff} = 7690^{+400}_{-250}$ K, $\log g = 4.15 \pm 0.04$ (where g is in units of cm s^{-2}), and $[\mathrm{Fe/H}] = 0.43^{+0.20}_{-0.28}$ dex. The effective temperature found for this star makes it one of the hottest known exoplanet hosts. The only known host stars hotter than TOI-1431 are KELT-9 ($T_{\rm eff} = 10{,}170 \pm 450$ K, Gaudi et al. 2017), WASP-178 ($T_{\rm eff} = 9360 \pm 150$ K, Hellier et al. 2019), KELT-20 ($T_{\rm eff} = 8720^{+250}_{-260}$ K, Lund et al. 2017), Kepler-1115 ($T_{\rm eff} = 8480^{+300}_{-220}$ K, Morton et al. 2016), HAT-P-70 ($T_{\rm eff} = 8450^{+540}_{-690}$ K, Zhou et al. 2019a), HATS-70 ($T_{\rm eff} = 7930^{+630}_{-820}$ K, Zhou et al. 2019b), and MASCARA-4 ($T_{\rm eff} = 7800 \pm 200$ K, Dorval et al. 2020). These stellar parameters (in particular $T_{\rm eff}$, $\log g$, and metallicity), however, are in strong disagreement with the spectroscopic parameters derived from the analysis of the SONG, SOPHIE, and FIES data. The source of this disagreement is likely due to the "anomalous luminosity effect" observed in Am stars (e.g., Bolton 1971) such as TOI-1431, which we discuss further in Section 5.1. The $\log g$ derived from the SED fit is in good agreement with the value obtained from the stellar density ($\log g \sim 4.17$ dex) from fitting the transits, and we have therefore adopted this value along with the values for $T_{\rm eff}$, $R_\star$, and $M_\star$ as the preferred values for the star.

Table 1
Stellar Parameters for HD 201033 as Used in This Work

Parameter	Value	Source
R.A. (hh:mm:ss)	21:04:48.89	(1) Gaia DR2
Decl. (dd:mm:ss)	55:35:16.88	(1) Gaia DR2
μ_α (mas yr^{-1})	11.74 ± 0.08	(1) Gaia DR2
μ_δ (mas yr^{-1})	23.87 ± 0.06	(1) Gaia DR2
Parallax (mas)	6.686 ± 0.046	(1) Gaia DR2
Luminosity ($L_\odot$)	10.69 ± 0.10[b]	(1) Gaia DR2
A_V (mag)	1.099 ($\leqslant$3.491)[c]	(2) Schlegel dust maps
Distance (pc)	$149.6^{+1.1}_{-1.0}$	(1) Gaia DR2
Spectral type	Am C (kA5mF2)	(3, 4, 5) A-type star catalogs
Broadband magnitudes:		
B_T (mag)	8.368 ± 0.016	(6) Tycho
V_T (mag)	8.049 ± 0.011	(6) Tycho
TESS (mag)	7.798 ± 0.006	(7) TESS TIC v8
J (mag)	7.541 ± 0.030	(8) 2MASS
H (mag)	7.452 ± 0.040	(8) 2MASS
K_s (mag)	7.439 ± 0.030	(8) 2MASS
WISE1 (mag)	7.335 ± 0.034	(9) WISE
WISE2 (mag)	7.430 ± 0.019	(9) WISE
WISE3 (mag)	7.446 ± 0.015	(9) WISE
WISE4 (mag)	7.371 ± 0.096	(9) WISE
Gaia (mag)	7.976 ± 0.001	(1) Gaia DR2
GaiaBP (mag)	8.123 ± 0.001	(1) Gaia DR2
GaiaRP (mag)	7.772 ± 0.001	(1) Gaia DR2
Stellar properties from SED and YY tracks:		
$T_{\rm eff}$ (K)	7690^{+400}_{-250}[a] [b]	(10) EXOFASTv2; this paper
$\log g$ (dex)	4.15 ± 0.04[b]	(10) EXOFASTv2; this paper
[Fe/H] (dex)	$0.43^{+0.20}_{-0.28}$	(10) EXOFASTv2; this paper
$R_\star$ ($R_\odot$)	1.92 ± 0.07[a] [b]	(10) EXOFASTv2; this paper
$M_\star$ ($M_\odot$)	$1.90^{+0.10}_{-0.08}$[a] [b]	(10) EXOFASTv2; this paper
$\rho_\star$ (g cm^{-3})	0.38 ± 0.05	(10) EXOFASTv2; this paper
$L_\star$ ($L_\odot$)	$11.7^{+2.3}_{-1.2}$	(10) EXOFASTv2; this paper
Age (Gyr)	$0.29^{+0.32}_{-0.19}$[b]	(10) EXOFASTv2; this paper
Spectroscopic properties from SONG spectra:		
$T_{\rm eff}$ (K)	6764 ± 120	(11, 12) iSpec; this paper
$\log g$ (dex)	2.76 ± 0.26	(11, 12) iSpec; this paper
[M/H] (dex)	-0.15 ± 0.10	(11, 12) iSpec; this paper
[α/H] (dex)	-0.27 ± 0.10	(11, 12) iSpec; this paper
$v \sin i$ (km s^{-1})	7.1 ± 1.0	(11, 12) iSpec; this paper
Spectroscopic properties from SOPHIE spectra:		
$T_{\rm eff}$ (K)	6950 ± 60	(13) FASMA; this paper
$\log g$ (dex)	4.72 ± 0.08	(13) FASMA; this paper
[Fe/H] (dex)	0.09 ± 0.03[b]	(13) FASMA; this paper
$v \sin i$ (km s^{-1})	6.0 ± 0.2[b]	CCF; this paper
Spectroscopic properties from FIES spectra:		
$T_{\rm eff}$ (K)	6910 ± 50	(14) SPC; this paper
$\log g$ (dex)	3.29 ± 0.10	(14) SPC; this paper
[M/H] (dex)	0.03 ± 0.08	(14) SPC; this paper
$v \sin i$ (km s^{-1})	9.2 ± 0.5	(14) SPC; this paper

Notes. 1. Gaia Collaboration et al. (2018); 2. Schlafly & Finkbeiner (2011); 3. Figueras et al. (1991); 4. Renson et al. (1991); 5. Renson & Manfroid (2009); 6. Høg et al. (2000); 7. Stassun et al. (2019); 8. Cutri et al. (2003); 9. Cutri et al. (2013); 10. Eastman et al. (2019); 11. Blanco-Cuaresma et al. (2014); 12. Blanco-Cuaresma (2019); 13. Tsantaki et al. (2018); 14. Buchhave et al. (2012).
[a] Priors used in the Allesfitter analysis.
[b] Preferred solution for the stellar and spectroscopic parameters.
[c] Upper limit on the V-band extinction from Schlegel dust maps.

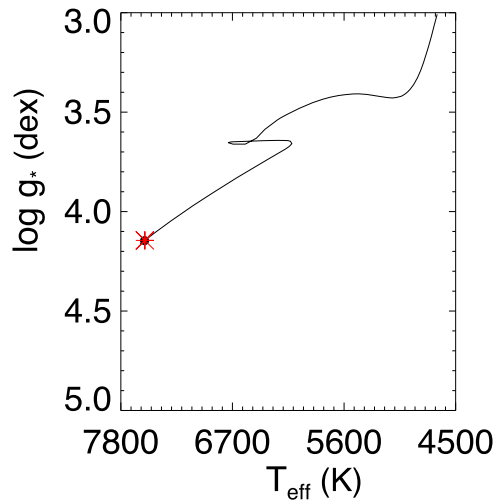

Figure 8. The YY mass track for TOI-1431. The black line represents the mass track interpolated at the model values for $M_\star$, [Fe/H], and age. The black circle is the best-fit model value for $T_{\rm eff}$ and $\log g$ while the red asterisk is the best-fit model age along the track. The black circle and red asterisk almost perfectly overlap, indicating excellent consistency among all the components of the global model.

3.2. Spectroscopy

We used the ISPEC spectral analysis tool (Blanco-Cuaresma et al. 2014; Blanco-Cuaresma 2019) to derive the effective temperature, surface gravity, rotational velocity, alpha elemental abundance ([α/H]), and overall metallicity ([M/H]) of TOI-1431 from the reduced and stacked SONG spectra. The ISPEC synthetic grid was configured to incorporate a MARCS atmospheric model (Gustafsson et al. 2008) and the SPECTRUM (Gray & Corbally 1994) radiative transfer code. [M/H] and [α/H] were derived using version 5.0 of Gaia-ESO Survey's (GES) line list (Heiter et al. 2015) normalized by solar values obtained by Asplund et al. (2009). Initial values for $T_{\rm eff}$, $\log g$, and [M/H] as determined by the SED analysis with EXOFASTv2 (see Section 3.1) were used to construct the synthetic spectral fit. From the ISPEC analysis of the SONG spectra, we find that TOI-1431 has $T_{\rm eff} = 6764 \pm 120$ K, $\log g = 2.76 \pm 0.26$ dex, [M/H] $= -0.15 \pm 0.10$ dex, [α/H] $= -0.27 \pm 0.10$ dex, and $v \sin i = 7.1 \pm 1.0$ km s^{-1}. These results would seem to suggest that the star is quite evolved, is slightly metal-poor, and is deficient in α elements. However, $T_{\rm eff}$ and $\log g$, in particular, are in very strong disagreement with the results obtained from the SED analysis as a consequence of the nature of the host being an Am star (see discussion in Section 5.1).

The atmospheric stellar parameters $T_{\rm eff}$, $\log g$, and [Fe/H] were derived from the SOPHIE spectra for TOI-1431 using the FASMA spectral synthesis package (Tsantaki et al. 2018). We provided initial stellar parameters for $T_{\rm eff}$, $\log g$, and [Fe/H] from the SED analysis with EXOFASTv2 as a starting point for the spectral synthesis in FASMA. The synthetic spectra were created using the radiative transfer code MOOG (Sneden 1973), and the grid of model atmospheres was generated by the ATLAS-APOGEE (Kurucz 1993), MARCS (Gustafsson et al. 2008), and ATLAS9 (Mészáros et al. 2012) models. The line list used to determine the stellar parameters comes from the Vienna Atomic Line Database (Piskunov et al.

1995; Ryabchikova et al. 2015) and includes all of the iron lines in the regions 5399–5619 Å and 6347–6790 Å as well as all the atomic and molecular lines within intervals of ±2 Å of the iron lines. From this analysis with the SOPHIE spectra, we find the star has $T_{\rm eff} = 6950 \pm 60$ K, $\log g = 4.72 \pm 0.08$ dex, and $[{\rm Fe/H}] = 0.09 \pm 0.03$ dex, consistent with a late A-type main-sequence star that is modestly metal-rich. We have adopted the [Fe/H] value derived here as the preferred value for the star's iron abundance.

The stellar parameters for this star were also derived from the FIES spectra using the stellar parameter classification (SPC) technique (Torres et al. 2012; Buchhave et al. 2012, 2014). To derive $T_{\rm eff}$, $\log g$, $v \sin i$, and [M/H] for this star using SPC, we cross-correlated the reduced and the stacked FIES spectra against a library of synthetic spectra calculated from the Kurucz model atmospheres (Castelli & Kurucz 2003). The synthetic spectra cover the wavelength range 5050–5360 Å; five of the FIES echelle orders span that region and could be used for the spectral analysis. The best-fit values were determined by finding the maximum of the cross-correlation coefficient as a function of the stellar parameters. The results of the SPC analysis on the FIES spectra give $T_{\rm eff} = 6910 \pm 50$ K, $\log g = 3.29 \pm 0.10$ dex, $[{\rm M/H}] = 0.03 \pm 0.08$ dex, and $v \sin i = 9.2 \pm 0.5\ {\rm km\,s^{-1}}$, which suggest an A-type subgiant star with solar metallicity. It should be noted that SPC was not designed for hot stars such as TOI-1431 and that surface gravities are often poorly constrained by spectral analyses (e.g., see Sozzetti et al. 2007; Winn et al. 2008).

The spectral analyses carried out on the SONG, SOPHIE, and FIES spectra give significantly different results for the host star properties, and in particular for the surface gravity. However, the stellar density (and surface gravity) determined from the SED and transit light-curve analysis are in good agreement with each other. Winn et al. (2008) has demonstrated that stellar densities can be more accurately determined through transit light-curve analysis and should be preferred over those derived through spectroscopy if there are strong disagreements between them. In this light, we therefore have adopted the $T_{\rm eff}$, $\log g$, $R_\star$, and $M_\star$ from the SED analysis as the preferred values for the star.

4. Modelling and Results

To determine the system parameters for TOI-1431 and its planet, including the planet's thermal emissions and day/night temperature contrast, we used `Allesfitter` (Günther & Daylan 2019, 2021) to perform a joint analysis of the TESS light-curve segments (from the multiscale MAP PDC, single-scale MAP PDC, and SAP photometry), the photometric ground-based light curves, and the radial velocity measurements. The ground-based light curves included in the analysis are from CDK14 (Sloan g' and z_s bands) taken on 2019 December 24, MuSCAT2 (four Sloan bands g', r', i', and z_s) obtained on 2020 May 16, AUKR (Sloan z_s band) observed on 2020 June 16, SCT (TESS-equivalent band) acquired on 2020 August 8, ULMT in the Sloan z' band collected on 2020 September 20, and LCOGT captured on 2020 October 14. We used the radial velocity measurements from the SONG, SOPHIE, FIES, NRES, and EXPRES instruments in the joint analysis.

4.1. Joint Transit, Phase-curve, and Radial Velocity Analysis

For the joint analysis, Gaussian priors were placed on the stellar parameters $R_\star$, $M_\star$, and $T_{\rm eff}$ from the SED and YY isochrones fitting using `EXOFASTv2`. We also applied a Gaussian prior on the dilution parameter (D_0) from the TESS SPOC light-curve parameter CROWDSAP, after transforming the CROWDSAP value to conform to the definition of the dilution parameter used in `Allesfitter` ($D_0 = 1 -$ CROWDSAP). For the other physical model parameters, we used uniform priors with reasonable boundaries and starting values. These parameters include the planet-to-star radius ratio ($R_{\rm p}/R_\star$), the ratio of the sum of the planet and star radii to the semimajor axis ($(R_\star + R_{\rm p})/a_{\rm p}$), cosine of the inclination angle ($\cos i_{\rm p}$), mid-transit time ($T_{0;b}$), orbital period ($P_{\rm p}$), the radial velocity semiamplitude (K), eccentricity ($\sqrt{e_{\rm p}} \cos \omega_{\rm p}$ and $\sqrt{e_{\rm p}} \sin \omega_{\rm p}$), surface brightness ratio ($J_{\rm p}$), set of quadratic limb-darkening coefficients (q_1 and q_2) and flux error scaling ($\ln \sigma_{F_{\rm inst}}$) for each of the light curves, and a radial velocity baseline offset ($\Delta{\rm RV}_{\rm inst}$) and jitter term ($\log \sigma_{{\rm RV}_{\rm inst}}$) for each radial velocity instrument.

We experimented with several different detrending techniques in our analysis of each of the three versions of the TESS photometry, including (1) baseline flux offset, (2) rspline detrending prior to the light-curve fitting with a baseline flux offset, (3) hybrid cubic spline detrending run simultaneously with the light-curve fitting, and (4) a red noise detrending model using a Matérn 3/2 Gaussian process (GP) kernel run simultaneously with the light-curve fitting. For the GP parameters, we applied uniform priors with reasonable boundaries and starting values on the flux offset (${\rm GP}_{\rm offset}$, between −0.01 and 0.01), characteristic amplitude ($\ln \sigma_{\rm flux}$, between −15 and 0), and characteristic length scale ($\ln \rho_{\rm flux}$, between 2.07 and 12). These parameters were also coupled across the TESS light-curve segments so that a single GP model is sampled at every sampling step. The lower boundary on the characteristic length-scale term was set to three times the planet's orbital period to ensure that the GP preserves any phase-curve modulations while still removing most of the remaining systematics present in the light-curve segments.

Close inspection of the TESS light curves reveals periodic photometric modulations that are synchronized with the orbital period of the planet. These phase-curve variations are driven by the changing viewing angle of the planet and the planet–star gravitational interaction. There are three main components to the phase curve that can be detected in visible-light photometry (see detailed review in Shporer 2017): (1) the atmospheric brightness modulation, which arises due to the variations in atmospheric temperature, thermal emission, and reflected starlight across the surface of a tidally locked planet, (2) ellipsoidal distortion of the host star due to the tidal bulge raised by the orbiting planet, and (3) beaming, i.e., modulations in the star's flux within the bandpass due primarily to the radial velocity-driven Doppler shifting of the stellar spectrum. Setting the zero-point of orbital phase at mid-transit, these three phase-curve modulations appear, to the leading order, as the cosine of the fundamental frequency, the cosine of the first harmonic, and the sine of the fundamental.

In this work, we also fit for these phase-curve terms by including free parameters for the respective full amplitudes: $A_{\rm atmospheric}$, $A_{\rm ellipsoidal}$, and $A_{\rm beaming}$. Similar methodologies have been used in extensive previous phase-curve analyses of TESS-observed exoplanet systems (e.g., Shporer et al. 2019;

Table 2
Priors Used in the Analysis

Parameter	Description	Prior[a]	Value
		Fitted parameters	
$R_b/R_\star$	Radius ratio	$\mathcal{U}(0.082; 0.010; 0.300)$	$0.07955^{+0.00063}_{-0.00053}$
$(R_\star + R_b)/a$	Radii sum to semimajor axis	$\mathcal{U}(0.21; 0.05; 0.50)$	0.2096 ± 0.0017
$\cos i_b$	Cosine of inclination	$\mathcal{U}(0.169; 0; 1)$	0.1715 ± 0.0022
T_0	Mid-transit time (2,458,700 – BJD_{TDB})	$\mathcal{U}(39.177; 38.177; 40.177)$	39.17737 ± 0.00007
P_b	Orbital period (d)	$\mathcal{U}(2.65; 2.35; 2.95)$	2.650237 ± 0.000003
$\sqrt{e}\cos\omega$	Eccentricity term	$\mathcal{U}(0.0; -0.3; 0.3)$	$-0.009^{+0.023}_{-0.021}$
$\sqrt{e}\sin\omega$	Eccentricity term	$\mathcal{U}(0.0; -0.3; 0.3)$	$0.036^{+0.033}_{-0.041}$
K_b	RV semiamplitude (km s^{-1})	$\mathcal{U}(0.300; 0; 1.0)$	0.2941 ± 0.0011
$D_{0_{TESS}}$	Dilution	$\mathcal{N}(0.004904; 0.000588)$	0.00486 ± 0.00051
$q_{1_{TESS}}$	Transformed limb darkening	$\mathcal{U}(0.40; 0; 1)$	0.22 ± 0.05
$q_{2_{TESS}}$	Transformed limb darkening	$\mathcal{U}(0.21; 0; 1)$	$0.18^{+0.13}_{-0.09}$
$q_{1_{LCO\ Y}}$	Transformed limb darkening	$\mathcal{U}(0.24; 0; 1)$	$0.19^{+0.13}_{-0.10}$
$q_{2_{LCO\ Y}}$	Transformed limb darkening	$\mathcal{U}(0.44; 0; 1)$	0.50 ± 0.29
$q_{1_{MuSCAT2\ z'}}$	Transformed limb darkening	$\mathcal{U}(0.35; 0; 1)$	$0.26^{+0.12}_{-0.10}$
$q_{2_{MuSCAT2\ z'}}$	Transformed limb darkening	$\mathcal{U}(0.42; 0; 1)$	0.52 ± 0.28
$q_{1_{MuSCAT2\ r'}}$	Transformed limb darkening	$\mathcal{U}(0.50; 0; 1)$	$0.41^{+0.13}_{-0.12}$
$q_{2_{MuSCAT2\ r'}}$	Transformed limb darkening	$\mathcal{U}(0.47; 0; 1)$	0.51 ± 0.25
$q_{1_{MuSCAT2\ i'}}$	Transformed limb darkening	$\mathcal{U}(0.26; 0; 1)$	$0.19^{+0.09}_{-0.08}$
$q_{2_{MuSCAT2\ i'}}$	Transformed limb darkening	$\mathcal{U}(0.53; 0; 1)$	$0.58^{+0.24}_{-0.28}$
$q_{1_{MuSCAT2\ g'}}$	Transformed limb darkening	$\mathcal{U}(0.62; 0; 1)$	$0.54^{+0.13}_{-0.11}$
$q_{2_{MuSCAT2\ g'}}$	Transformed limb darkening	$\mathcal{U}(0.61; 0; 1)$	$0.63^{+0.19}_{-0.21}$
$q_{1_{ULMT\ i'}}$	Transformed limb darkening	$\mathcal{U}(0.26; 0; 1)$	$0.14^{+0.18}_{-0.10}$
$q_{2_{ULMT\ i'}}$	Transformed limb darkening	$\mathcal{U}(0.53; 0; 1)$	$0.35^{+0.32}_{-0.23}$
$q_{1_{CDK14\ z'}}$	Transformed limb darkening	$\mathcal{U}(0.35; 0; 1)$	0.54 ± 0.28
$q_{2_{CDK14\ z'}}$	Transformed limb darkening	$\mathcal{U}(0.42; 0; 1)$	0.51 ± 0.30
$q_{1_{CDK14\ g'}}$	Transformed limb darkening	$\mathcal{U}(0.62; 0; 1)$	$0.45^{+0.29}_{-0.27}$
$q_{2_{CDK14\ g'}}$	Transformed limb darkening	$\mathcal{U}(0.61; 0; 1)$	$0.63^{+0.23}_{-0.31}$
$q_{1_{AUKR\ z'}}$	Transformed limb darkening	$\mathcal{U}(0.35; 0; 1)$	$0.83^{+0.11}_{-0.18}$
$q_{2_{AUKR\ z'}}$	Transformed limb darkening	$\mathcal{U}(0.42; 0; 1)$	$0.60^{+0.24}_{-0.29}$
$q_{1_{SCTTESS}}$	Transformed limb darkening	$\mathcal{U}(0.40; 0; 1)$	$0.22^{+0.15}_{-0.11}$
$q_{2_{SCTTESS}}$	Transformed limb darkening	$\mathcal{U}(0.21; 0; 1)$	$0.57^{+0.26}_{-0.30}$
J_p	Surface brightness ratio	$\mathcal{U}(0.0074; 0; 0.1)$	0.0076 ± 0.0023
$A_{beaming}$	Phase curve term (ppt)	$\mathcal{U}(0.0099; 0; 1)$	$0.0010^{+0.0012}_{-0.0007}$
$A_{atmospheric}$	Phase curve term (ppt)	$\mathcal{U}(0.0976; 0; 1)$	$0.0785^{+0.0073}_{-0.0077}$
$A_{ellipsoidal}$	Phase curve term (ppt)	$\mathcal{U}(0.0409; 0; 1)$	0.0291 ± 0.0064
$\ln\sigma_{TESS}$	Flux error scaling (ln rel. flux)	$\mathcal{U}(-7.545; -10; -5)$	$-7.779^{+0.003}_{-0.004}$
$\ln\sigma_{LCO\ Y}$	Flux error scaling (ln rel. flux)	$\mathcal{U}(-6.53; -10; -3)$	-6.528 ± 0.040
$\ln\sigma_{MuSCAT2\ z'}$	Flux error scaling (ln rel. flux)	$\mathcal{U}(-6.92; -10; -3)$	-6.926 ± 0.041
$\ln\sigma_{MuSCAT2\ r'}$	Flux error scaling (ln rel. flux)	$\mathcal{U}(-7.00; -10; -3)$	-7.007 ± 0.041
$\ln\sigma_{MuSCAT2\ i'}$	Flux error scaling (ln rel. flux)	$\mathcal{U}(-7.02; -10; -3)$	-7.019 ± 0.041
$\ln\sigma_{MuSCAT2\ g'}$	Flux error scaling (ln rel. flux)	$\mathcal{U}(-7.05; -10; -3)$	-7.045 ± 0.042
$\ln\sigma_{ULMT\ i'}$	Flux error scaling (ln rel. flux)	$\mathcal{U}(-6.5; -10; -3)$	-5.826 ± 0.030
$\ln\sigma_{CDK14\ z'}$	Flux error scaling (ln rel. flux)	$\mathcal{U}(-5.9; -10; -3)$	-5.330 ± 0.043
$\ln\sigma_{CDK14\ g'}$	Flux error scaling (ln rel. flux)	$\mathcal{U}(-6.1; -10; -3)$	-5.358 ± 0.044
$\ln\sigma_{AUKR\ z'}$	Flux error scaling (ln rel. flux)	$\mathcal{U}(-5.8; -10; -3)$	5.808 ± 0.031
$\ln\sigma_{SCTTESS}$	Flux error scaling (ln rel. flux)	$\mathcal{U}(-6.5; -10; -3)$	-5.845 ± 0.023
$\log\sigma_{RV_{SONG}}$	RV jitter (km s^{-1})	$\mathcal{U}(-7.35; -10; -1)$	-7.2 ± 1.6
$\log\sigma_{RV_{ELP}}$	RV jitter (km s^{-1})	$\mathcal{U}(-2.93; -10; -1)$	$-2.97^{+0.34}_{-0.31}$
$\log\sigma_{RV_{TLV}}$	RV jitter (km s^{-1})	$\mathcal{U}(-2.79; -10; -1)$	$-2.79^{+0.14}_{-0.14}$
$\log\sigma_{RV_{FIES}}$	RV jitter (km s^{-1})	$\mathcal{U}(-4.43; -10; -1)$	$-7.3^{+1.3}_{-1.5}$
$\log\sigma_{RV_{SOPHIE}}$	RV jitter (km s^{-1})	$\mathcal{U}(-5.09; -10; -1)$	$-5.54^{+0.73}_{-1.3}$
$\log\sigma_{RV_{EXPRES}}$	RV jitter (km s^{-1})	$\mathcal{U}(-2.50; -10; -1)$	$-7.15^{+0.70}_{-1.1}$
ΔRV_{SONG}	RV offset (km s^{-1})	$\mathcal{U}(-25.15; -26.0; -24.4)$	-25.154 ± 0.006
ΔRV_{ELP}	RV offset (km s^{-1})	$\mathcal{U}(-25.57; -26.5; -24.8)$	-25.579 ± 0.019

Table 2
(Continued)

Parameter	Description	Prior[a]	Value
ΔRV_{TLV}	RV offset (km s^{-1})	$\mathcal{U}(-25.56; -26.0; -25.0)$	-25.570 ± 0.011
ΔRV_{FIES}	RV offset (km s^{-1})	$\mathcal{U}(-0.28; -1.2; 0.2)$	-0.274 ± 0.002
ΔRV_{SOPHIE}	RV offset (km s^{-1})	$\mathcal{U}(-25.24; -26.0; -24.4)$	-25.249 ± 0.003
ΔRV_{EXPRES}	RV offset (km s^{-1})	$\mathcal{U}(0.0; -1.0; 1.0)$	0.0051 ± 0.0007
	Derived parameters		
$R_\star/a$	Host radius to semimajor axis		0.194 ± 0.002
$a/R_\star$	Semimajor axis to host radius		5.15 ± 0.05
R_b	Planet radius ($R_\oplus$)		16.7 ± 0.6
R_b	Planet radius (R_J)		1.49 ± 0.05
a	Semimajor axis (au)		0.046 ± 0.002
i	Inclination (deg)		80.13 ± 0.13
b_{tra}	Impact parameter		0.881 ± 0.004
e	Eccentricity		$0.0022^{+0.0030}_{-0.0016}$
ω	Argument of periastron (deg)		108^{+92}_{-31}
q_b	Mass ratio		0.00157 ± 0.00006
M_b	Companion mass ($M_\oplus$)		990 ± 60
M_b	Companion mass (M_J)		3.12 ± 0.18
T_{tot}	Total transit duration (h)		2.489 ± 0.009
T_{full}	Full-transit duration (h)		1.057 ± 0.034
$T_{0;occ}$	Epoch occultation (2,458,700 – BJD_{TDB})		40.502 ± 0.002
b_{occ}	Impact parameter occultation		$0.885^{+0.006}_{-0.005}$
$\rho_\star$	Host density from orbit (cgs)		0.37 ± 0.01
ρ_b	Companion density (cgs)		$1.17^{+0.18}_{-0.16}$
g_b	Companion surface gravity (cgs)		3430^{+50}_{-60}
T_{eq}[b]	Equilibrium temperature (K)		2370 ± 70
H_b	Companion atmospheric scale height (km)		230 ± 30
$u_{1;TESS}$	Limb darkening		$0.13^{+0.13}_{-0.08}$
$u_{2;TESS}$	Limb darkening		$0.33^{+0.10}_{-0.12}$
$u_{1;LCO\ Y}$	Limb darkening		$0.40^{+0.27}_{-0.24}$
$u_{2;LCO\ Y}$	Limb darkening		$0.00^{+0.25}_{-0.22}$
$u_{1;MuSCAT2\ z'}$	Limb darkening		0.51 ± 0.26
$u_{2;MuSCAT2\ z'}$	Limb darkening		$-0.02^{+0.29}_{-0.24}$
$u_{1;MuSCAT2\ r'}$	Limb darkening		$0.64^{+0.28}_{-0.31}$
$u_{2;MuSCAT2\ r'}$	Limb darkening		$-0.01^{+0.33}_{-0.28}$
$u_{1;MuSCAT2\ i'}$	Limb darkening		0.49 ± 0.24
$u_{2;MuSCAT2\ i'}$	Limb darkening		$-0.07^{+0.24}_{-0.20}$
$u_{1;MuSCAT2\ g'}$	Limb darkening		$0.91^{+0.25}_{-0.28}$
$u_{2;MuSCAT2\ g'}$	Limb darkening		$-0.18^{+0.31}_{-0.26}$
$u_{1;ULMT\ i'}$	Limb darkening		$0.23^{+0.25}_{-0.16}$
$u_{2;ULMT\ i'}$	Limb darkening		$0.09^{+0.23}_{-0.19}$
$u_{1;CDK14\ z'}$	Limb darkening		$0.67^{+0.50}_{-0.40}$
$u_{2;CDK14\ z'}$	Limb darkening		$-0.02^{+0.42}_{-0.39}$
$u_{1;CDK14\ g'}$	Limb darkening		$0.76^{+0.46}_{-0.43}$
$u_{2;CDK14\ g'}$	Limb darkening		$-0.15^{+0.35}_{-0.33}$
$u_{1;AUKR\ z'}$	Limb darkening		$1.04^{+0.44}_{-0.50}$
$u_{2;AUKR\ z'}$	Limb darkening		$-0.17^{+0.51}_{-0.42}$
$u_{1;SCT\{TESS}$	Limb darkening		$0.48^{+0.27}_{-0.24}$
$u_{2;SCT\{TESS}$	Limb darkening		$-0.05^{+0.29}_{-0.21}$
$\delta_{TESS_{tr};undil}$	Transit depth (undil.) (ppt)		5.825 ± 0.007
$\delta_{TESS_{tr};dil}$	Transit depth (dil.) (ppt)		5.797 ± 0.007
$\delta_{TESS_{occ};undil}$	Occultation depth (undil.) (ppt)		$0.127^{+0.004}_{-0.005}$
$\delta_{TESS_{occ};dil}$	Occultation depth (dil.) (ppt)		$0.127^{+0.004}_{-0.005}$
$F_{TESS_{night};undil}$	Nightside flux (undil.) (ppt)		$0.049^{+0.004}_{-0.005}$
$F_{TESS_{night};dil}$	Nightside flux (dil.) (ppt)		$0.049^{+0.004}_{-0.005}$
$\delta_{LCO\ Y}$	Transit depth (ppt)		$5.67^{+0.25}_{-0.27}$
$\delta_{MuSCAT2\ z'}$	Transit depth (ppt)		$5.54^{+0.22}_{-0.24}$
$\delta_{MuSCAT2\ r'}$	Transit depth (ppt)		$5.30^{+0.22}_{-0.27}$

Table 2
(Continued)

Parameter	Description	Prior[a]	Value
$\delta_{\mathrm{MuSCAT2\ i'}}$	Transit depth (ppt)		$5.62^{+0.21}_{-0.23}$
$\delta_{\mathrm{MuSCAT2\ g'}}$	Transit depth (ppt)		4.90 ± 0.26
$\delta_{\mathrm{ULMT\ i'}}$	Transit depth (ppt)		$5.84^{+0.26}_{-0.31}$
$\delta_{\mathrm{CDK14\ z'}}$	Transit depth (ppt)		$5.13^{+0.47}_{-0.61}$
$\delta_{\mathrm{CDK14\ g'}}$	Transit depth (ppt)		$5.09^{+0.55}_{-0.68}$
$\delta_{\mathrm{AUKR\ z'}}$	Transit depth (ppt)		$4.51^{+0.53}_{-0.56}$
$\delta_{\mathrm{SCTTESS}}$	Transit depth (ppt)		$5.58^{+0.24}_{-0.27}$

Notes. Median values and 68% confidence intervals of the fitted and derived parameters for TOI-1431b from the joint nested sampling Allesfitter analysis of the TESS single-scale MAP corrected PDC photometry, ground-based light curves, and radial velocity measurement.
[a] $\mathcal{N}(\mu;\sigma)$ is a normal distribution with mean μ and width σ, $\mathcal{U}(s;a;b)$ is a uniform prior with a starting value s and lower and upper limits of a and b, respectively.
[b] Calculated assuming zero Bond albedo.

Wong et al. 2020a, 2020b, 2020c; Daylan et al. 2021). The full list of priors used in the analysis is given in Table 2.

4.1.1. Multiscale MAP PDC Photometry

We started the joint analysis using the TESS multiscale MAP corrected PDC light curve (after removing all quality-flagged data and outliers as described in Section 2.1) since most of the instrumental systematics are removed by the SPOC PDC pipeline from the use of cotrending basis vectors and flux corrections due to crowding from other stars (e.g., see Stumpe et al. 2014). This results in a cleaner light curve than the SAP version while still preserving astrophysical signals on time-scales shorter than the orbital period of TOI-1431b, important for phase-curve and secondary eclipse analysis.

The analysis was carried out using an MCMC process that ran until convergence (all chains are >42 times their autocorrelation lengths) for the four different detrending techniques mentioned in Section 4.1. Figure 9 is the resulting phase-folded and detrended PDC light curve of TOI-1431 from the hybrid cubic spline detrending, overplotted with 20 light-curve models drawn from the MCMC posteriors. It is apparent in the residuals to the best-fit transit model that there are two significant dip features in the light curve (∼200 ppm depth), one starting ∼1 hr before transit ingress and continuing until just after the start of ingress and another starting just prior to the end of egress with a duration of ∼1 hr. The residuals from the fit using the other three detrending techniques also show similar dip features. As additional checks, we ran the `Allesfitter` analysis without any detrending separately on the Sector 15 and 16 PDC light curves and observed similar dip signatures, ruling out the possibility that the light-curve detrending was responsible for these features. These signatures are also present in the DV light curve provided in the DV Report Summary available on exo.MAST.

Further investigations revealed the source of the dip features to be a wavelet artifact caused by the multiscale MAP correction applied by PDC (see Section 2.1). Normally, multiscale MAP performs better than single-scale MAP for removing long-period systematics while preserving signals at transit scales. However, there is a mechanism where multiscale MAP can slightly corrupt a very deep transit in a light curve with little long-period systematics, such as we see in TOI-1431. The single-scale MAP corrected light curve was found to not contain the dip features and, as such, we chose to report the results of the analysis performed on that light curve.

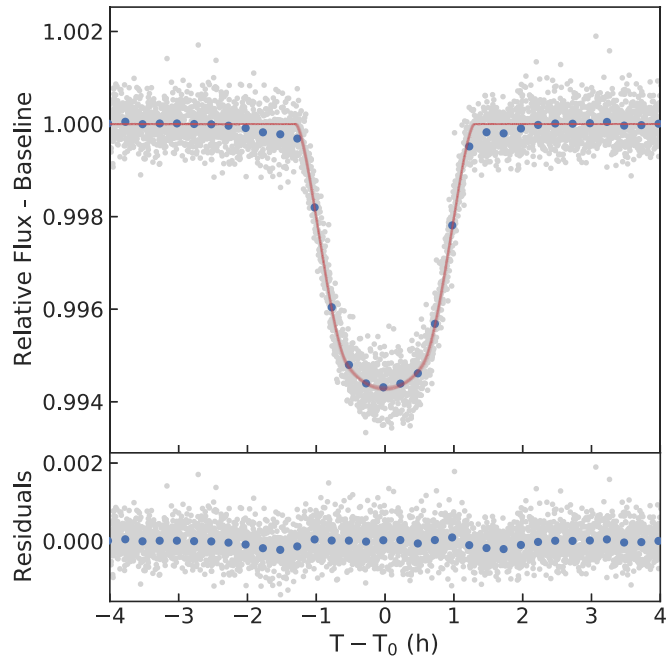

Figure 9. Phase-folded and detrended TESS multiscale MAP PDC light curve of TOI-1431 (Sectors 15 and 16) from the simultaneous hybrid cubic spline detrending model, focusing on the transit. Systematics and other quality-flagged data (as shown in Figure 1) that are the result of, for example, spacecraft pointing anomalies have been removed prior to performing the analysis on the light curve. The blue points are binned at a cadence of 15 minutes and the red solid lines are 20 light-curve models drawn from the posteriors of the Markov Chain Monte Carlo analysis in `Allesfitter`. Dip features starting ∼1 hr before and after transit ingress and egress, respectively, are apparent in the light curve and were introduced during the PDC multiscale MAP cotrending process. These dip features are not present in the single-scale MAP corrected PDC and SAP versions of the light curve (see Figure 10).

4.1.2. Single-scale MAP PDC Photometry

The joint analysis with the precleaned (as described in Section 2.1) single-scale MAP corrected PDC light-curve segments in `Allesfitter` follows the same procedure as with the multiscale MAP corrected PDC light curves. We ran MCMC fits until convergence for the four different detrending techniques. We then used the best-fit parameter values found from the MCMC as starting values in subsequent nested sampling fits to estimate the Bayesian evidence for use in a robust comparison of the four detrending models. We used the default `Allesfitter` settings for the nested sampling fits (see

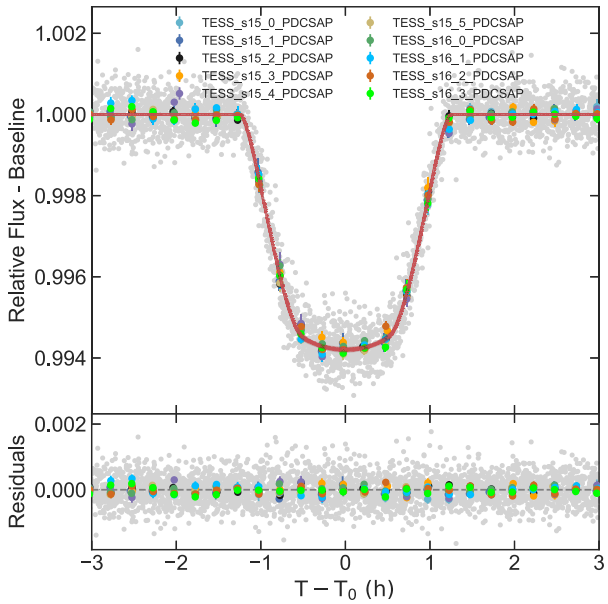

Figure 10. Phase-folded and detrended light curve of TOI-1431 from the simultaneous hybrid cubic spline detrending model, similar to Figure 9, but with the single-scale MAP corrected PDC data instead. The colored points represent the individual phased light-curve segments across Sectors 15 and 16 that have been binned at a cadence of 15 minutes. The red solid lines are 20 light-curve models drawn from the posteriors of the nested sampling analysis in `Allesfitter`.

(The data used to create this figure are available.)

Günther & Daylan 2021) that ran until they reached the convergence criterion threshold of $\Delta \ln Z \leqslant 0.01$.

The results from the nested sampling fits are in good agreement with the MCMC results to within 1σ. Comparing the Bayesian evidence of the nested sampling models, we find that the hybrid cubic spline detrending run simultaneously with the light-curve fitting is decisively favored over the second most favored model, the red noise GP detrending model, with a Bayes model comparison factor of $\ln R = 119$. We also applied the hybrid cubic spline detrending to each of the ground-based transit light curves used in the joint fit.

Figure 10 shows the resulting phase-folded and detrended single-scale MAP PDC light curve of TOI-1431 from the simultaneous cubic spline detrending nested sampling model. Unlike the multiscale MAP PDC light curve shown in Figure 9, there is no evidence of the strange dip features near the transit, motivating our decision to use the results derived from the single-scale MAP version of light-curve analysis.

Both the MCMC and nested sampling give consistent results, and we report both the fitted and derived parameter results of the nested sampling model in Table 2. In Figures 3, 4, and 5, we show the ground-based transit light curves and radial velocity measurements with the corresponding models drawn from the nested sampling posterior, respectively.

Our preferred solution from the joint analysis using the single-scale MAP PDC light curve shows that TOI-1431 hosts an inflated and highly irradiated Jovian planet with a radius of $R_p = 1.49 \pm 0.05\, R_J$ ($16.7 \pm 0.6\, R_\oplus$), mass of $3.12 \pm 0.18\, M_J$, high equilibrium temperature of $T_{eq} = 2370 \pm 70$ K (assuming zero Bond albedo), and a circular orbit with a period of $P = 2.650237 \pm 0.000003$ days. The mean density of the planet is $1.17^{+0.18}_{-0.16}$ g cm^{-3}, slightly less than but consistent with the density of Jupiter (1.326 g cm^{-3}) and similar to other Jovian worlds. The large number and high quality of radial velocity measurements (as shown in Figure 5), coupled with the host star's low $v \sin i$ of 6.0 ± 0.2 km s^{-1}, have allowed us to measure the radial velocity semiamplitude of the orbit (294.1 ± 1.1 m s^{-1}) with unusually high precision for a planet orbiting such a hot star (7690^{+400}_{-250} K). In fact, this is the highest precision orbit measured for any planet that has a host star hotter than 6600 K. The largest contributor to the uncertainty in the planet mass (17.4σ detection) is from the uncertainty on the host star mass.

There is also a clear signature of the secondary eclipse (occultation, i.e., when the planet passes behind the star) with a depth of $\delta_{occ;dil} = 0.127^{+0.004}_{-0.005}$ ppt. We also robustly detect the longitudinal modulation of the planet's light in the TESS bandpass ($A_{atmospheric} = 0.078^{+0.007}_{-0.008}$ ppt) from the full phase curve, as shown in Figure 11, providing us with a rare opportunity to measure the planet's day/night brightness temperature contrast (see Section 4.1).

From the light curve, we see a very weak beaming signal with a measured amplitude of $A_{beaming} = 0.0010^{+0.0012}_{-0.0006}$ ppt and a marginal detection of ellipsoidal modulation with an amplitude of $A_{ellipsoidal} = 0.029 \pm 0.006$ ppt. The predicted full amplitudes of both of these phase-curve components can be derived from theory and depend on the planet–star mass ratio $q_p = M_p/M_*$ (see, for example, the review in Shporer 2017):

$$A_{ellipsoidal} = 2\alpha_{ellip} q_p \left(\frac{R_*}{a}\right)^3 \sin^2 i_p, \tag{1}$$

$$A_{beaming} = 2\left[\frac{2\pi G}{P_p c^3}\frac{q_p^2 M_p \sin^3 i_p}{(1+q_p)^2}\right]^{1/3} \left\langle \frac{x e^x}{e^x - 1}\right\rangle_{TESS}. \tag{2}$$

Here, we have assumed for simplicity that the stellar spectrum is a blackbody, and $x \equiv hc/k\lambda T_*$; the angled brackets indicate averaging over the TESS bandpass. The prefactor α_{ellip} in the ellipsoidal distortion is an expression that includes the limb- and gravity-darkening coefficients for the host star.

To calculate the predicted amplitudes, we use the stellar parameters derived from the SED fit (Table 1) and the best-fit system parameters from the joint analysis. For the limb- and gravity-darkening coefficients, we take tabulated values from Claret (2017) and interpolate to the measured stellar parameters. Uncertainties are propagated to the estimates using Monte Carlo sampling. We obtain predicted amplitudes of $A_{ellipsoidal} = 0.028 \pm 0.004$ ppt and $A_{beaming} = 0.0052 \pm 0.0004$ ppt. These theoretical values are in excellent agreement with our measured values to within the 1σ level.

Our phase-curve analysis did not consider a possible phase shift in the time of maximum brightness, which would correspond to an offset in the dayside hotspot. Previous studies of ultrahot Jupiters have indicated very small (if any) phase-curve offsets (see, for example, the case of KELT-9 b; Wong et al. 2020b). Any offset would manifest itself in our phase-curve fits through its effect on the measured beaming amplitude. We have shown that the measured and predicted values of $A_{beaming}$ are consistent to within 1σ. Therefore, we conclude that there is no evidence for a significant phase offset in the planet's atmospheric brightness modulation.

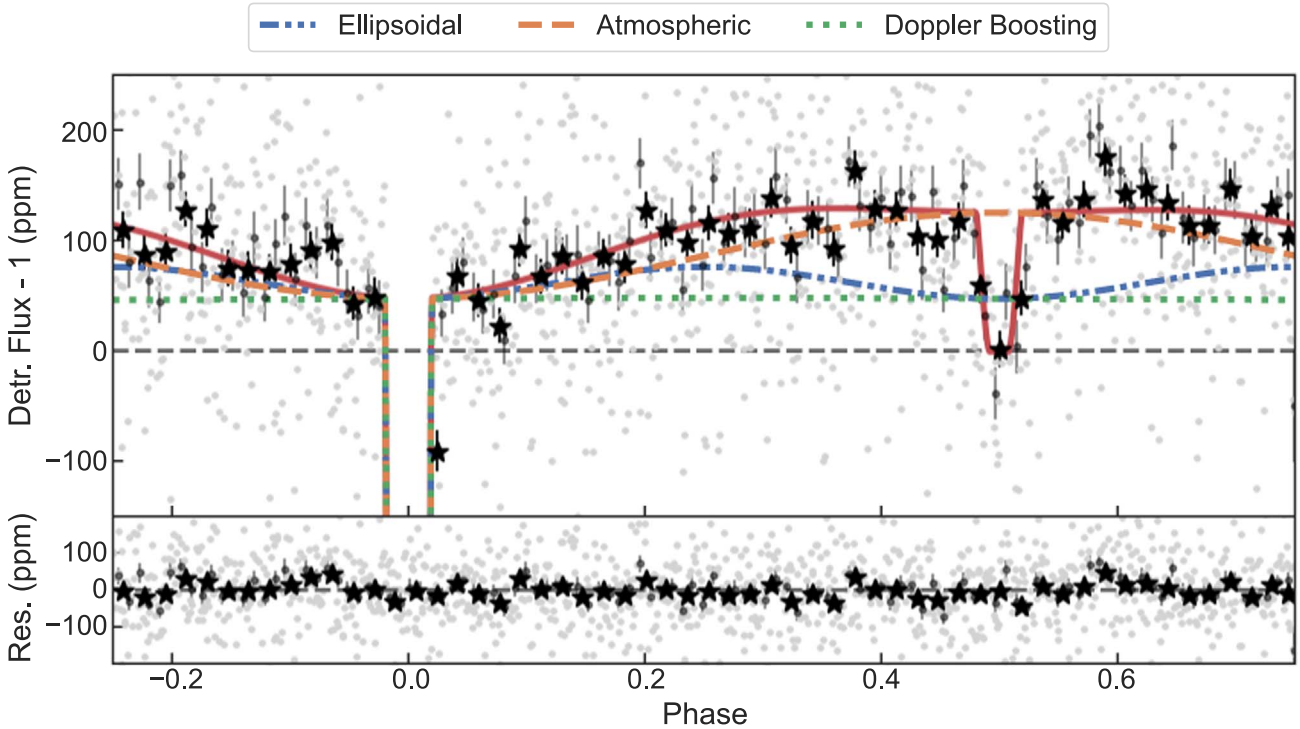

Figure 11. The phase-folded TESS single-scale MAP PDC light curve for TOI-1431b, zoomed in to show the phase curve and secondary eclipse. The gray points are the detrended photometry, the dark gray points are the binned photometry with a cadence of $P/300$ (∼12.7 minutes), and the black stars are the binned photometry with a cadence of $P/150$ (∼25.5 minutes). Included in the phase-curve model fit are the ellipsoidal (blue dashed–dotted line), the atmospheric (orange dashed line), and the beaming (green dotted line) modulations. The combined median model fit is plotted as the solid red line. The dark gray dashed line represents no emission from TOI-1431b. The bottom panel shows the residuals to the combined median model.

4.1.3. SAP Photometry

We also performed the analysis of the precleaned SAP light-curve segments following the same procedures as done in Sections 4.1.1 and 4.1.2. The SAP light curve (see Figure 15 in the Appendix) also shows no evidence of the dip features near the transit.

We do find some discrepancies in the results between the joint fit using the SAP light curve and the single-scale MAP PDC light curve that are likely due to spacecraft point excursions (see Figure 16 in the Appendix).

However, most of our derived parameters were consistent within 1σ. We adopt the results from the joint analysis using the single-scale MAP PDC light curve based on Bayesian model comparison for the discussion of this paper.

4.2. The Atmosphere

We have used the TESS single-scale MAP corrected PDC photometry and `Allesfitter` to characterize the red-optical (6000–9500 Å) phase curve of TOI-1431b, which includes contributions from beaming, ellipsoidal modulation, and atmospheric brightness modulation, as well as the secondary eclipse (see Section 4.1.2). We also fit the phase curve and secondary eclipse using the TESS SAP photometry (see Figure 18 in the Appendix) as a comparison to our preferred solution using the single-scale MAP PDC photometry.

From the measured secondary eclipse depth $\delta_{\rm occ}$ and nightside planetary flux $\delta_{\rm night}$, we can derive the dayside and nightside brightness temperatures of TOI-1431b using the relationship between the planet–star flux ratio δ, planetary emission $F_{\rm p}(\lambda, T_{\rm p})$ (assumed to be a blackbody), and stellar spectrum $F_*(\lambda, T_{\rm eff})$:

$$\delta = \left(\frac{R_{\rm p}}{R_*}\right)^2 \frac{\int F_{\rm p}(\lambda, T_{\rm p})\tau(\lambda)d\lambda}{\int F_*(\lambda, T_{\rm eff})\tau(\lambda)d\lambda} + A_{\rm g}\left(\frac{R_{\rm p}}{a}\right)^2. \quad (3)$$

Any light reflected by the dayside atmosphere contributes to the measured flux ratio through the geometric albedo $A_{\rm g}$; this second term is zero when computing the nightside temperature. The planetary and stellar spectra are integrated over the TESS bandpass, which has a transmission function (in energy units) represented by $\tau(\lambda)$.

We model the star's spectrum using PHOENIX models (Husser et al. 2013). To properly interpolate the stellar models and propagate the uncertainties in stellar parameters to the estimates of planetary temperature, we follow the methodology described in Wong et al. (2020b) and calculate the integrated stellar flux within the TESS bandpass for a grid of PHOENIX models, before fitting a cubic polynomial in ($T_{\rm eff}$, log g, [Fe/H]) to the full set of values. We then use a standard MCMC routine to compute the posterior distribution of the planetary brightness temperature $T_{\rm p}$, with Gaussian priors on the stellar and system parameters, as well as the measured dayside or nightside flux ($\delta_{\rm occ}$ or $\delta_{\rm night}$; see Table 2).

For the dayside brightness temperature, we obtain $T_{\rm day} = 3004 \pm 64$ K when assuming zero geometric albedo; across an albedo range of 0–0.2, we find dayside brightness temperatures spanning 2700–3100 K. We measure a very high nightside brightness temperature of $T_{\rm night} = 2583 \pm 63$ K. The extremely hot dayside is expected to preclude the formation of condensates, resulting in a cloud-free dayside hemisphere (e.g., Wakeford et al. 2017). Previous analyses of other ultrahot Jupiters combining secondary eclipses at optical and thermal

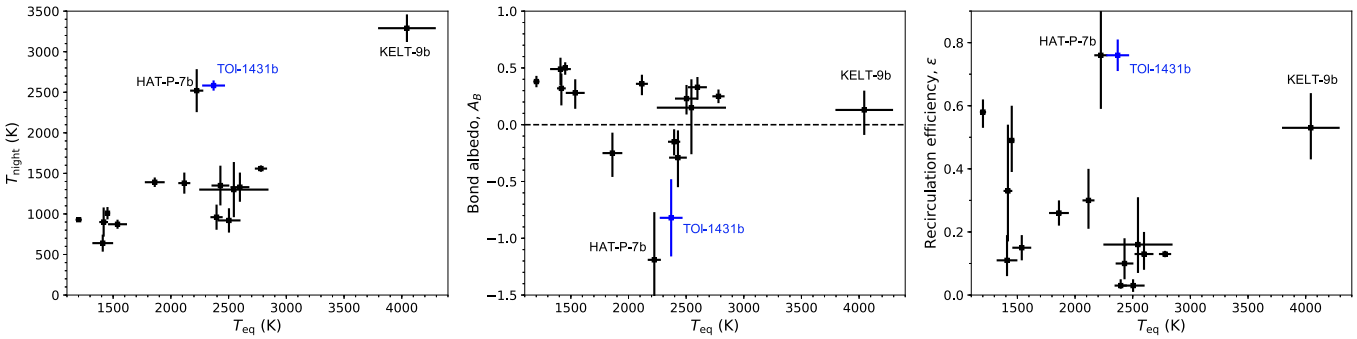

Figure 12. Plots of nightside brightness temperature T_{night}, Bond albedo A_B, and day–night heat recirculation efficiency ϵ as a function of equilibrium temperature T_{eq} for a population of hot and ultrahot Jupiters. TOI-1431b is indicated in blue; the black points are taken/derived from the results of Bell et al. (2021). KELT-16b has been omitted due to its very large nightside temperature uncertainty (>400 K) and poorly constrained ϵ value. With its high nightside temperature, low day/night temperature contrast, and strongly negative Bond albedo, TOI-1431b is a notable outlier among gas giants with similar levels of stellar irradiation, and is very similar to HAT-P-7b.

infrared wavelengths confirm the predictions of low reflectivity, yielding near-zero geometric albedos (e.g.,WASP-18b and WASP-33b; Shporer et al. 2019; von Essen et al. 2020).

We use the measured dayside and nightside brightness temperatures to jointly constrain the Bond albedo A_B and the efficiency of heat recirculation from the dayside to nightside of the planet ϵ (0 for no recirculation; 1 for full recirculation), following the thermal balance formalism outlined in Cowan & Agol (2011) and the methodology described in Wong et al. (2020b). We find $A_B = -0.82^{+0.30}_{-0.38}$ and $\epsilon = 0.76 \pm 0.05$. The very efficient day–night heat recirculation is borne out by the low day/night temperature contrast (~420 K). However, the unusual negative Bond albedo suggests that the overall thermal emission level across the entire planet cannot be accounted for by the energy input from stellar insolation alone.

By placing TOI-1431b in context, we can appreciate the exceptional atmospheric properties of this planet. Figure 12 shows the nightside brightness temperatures, Bond albedos, and recirculation efficiencies for a sample of hot and ultrahot Jupiters, taken and/or analogously derived from the brightness temperatures listed in the comprehensive Spitzer 4.5 μm phase-curve analysis by Bell et al. (2021). From the plots, it is evident that TOI-1431b has a much higher nightside temperature and day–night heat recirculation efficiency than most other hot Jupiters with comparable equilibrium temperatures. In particular, this planet has a higher heat recirculation efficiency and significantly lower Bond albedo than KELT-9 b ($\epsilon = 0.39 \pm 0.05$ and $A_B = 0.19^{+0.12}_{-0.11}$; Wong et al. 2020b), the hottest exoplanet ever discovered (Gaudi et al. 2017), with dayside and nightside brightness temperatures of $T_{day} = 4450^{+220}_{-210}$ K and $T_{night} = 3290 \pm 170$ K (Bell et al. 2021), respectively. Meanwhile, only HAT-P-7 b has a similar strongly (>2σ) negative inferred Bond albedo; indeed, HAT-P-7 b is very similar to TOI-1431b in all respects. Broadly speaking, KELT-9 b, HAT-P-7 b, and TOI-1431b are outliers amid the weak overall trends across gas giants with $T_{eq} > 1200$ K, i.e., increasing nightside temperature, decreasing Bond albedo, and decreasing day–night heat recirculation efficiency with increasing equilibrium temperature. In the case of KELT-9 b in particular, given its extreme dayside temperature, its anomalously high heat recirculation efficiency could be explained from the moderation of the day/night temperature contrast due to the transport of thermally dissociated atomic hydrogen from the dayside to the nightside and subsequent recombination into molecular hydrogen, which releases a significant amount of heat (e.g., Bell & Cowan 2018).

The unexpected negative Bond albedo may indicate the limitations of the simple thermal balance considerations underpinning our estimates of A_B and ϵ. In particular, gradients in chemical composition between the dayside and nightside hemispheres can entail drastically different atmospheric opacities, meaning that the pressure levels probed by our broadband photometric measurements may vary significantly across the planet's surface. Another explanation for a negative Bond albedo is additional thermal emission from residual heat of formation. This scenario would increase the emitted flux at all longitudes, raising the measured brightness temperatures on both the dayside and the nightside hemispheres.

This explanation may be especially applicable to TOI-1431b: the stellar age inferred from SED modeling is $0.29^{+0.32}_{-0.19}$ Gyr, making the system among the youngest hosting giant planets hitherto discovered. However, the age of the planet is sufficient for it to have deflated through the initial Kelvin–Helmholtz contraction phase and for its atmosphere to have cooled and reached the equilibrium temperature. The timescale over which this initial cooling and deflation occurred is ~1 Myr (see Equation (17) from Ginzburg & Sari 2015), the photospheric cooling time to reach the regime where stellar irradiation acts to slow cooling. The current level of incident stellar flux is sufficient to slow the planet's interior cooling and allow it to remain hot and inflated at its present-day radius (see Figure 17 in the Appendix and Komacek et al. 2020; Mol Lous & Miguel 2020). We do not require deposited heating in the deep interior to explain the present-day radius, however; a weak conversion of <0.05% of the incident stellar flux to deposited heating is allowed. Importantly, we find that the effects of irradiation slowing cooling can only explain the present-day radius if TOI-1431b arrived at its current orbit within ~1 Myr after formation. This may imply either that TOI-1431b formed in situ or that a nearby stellar or massive planetary companion rapidly scattered the planet inward very soon after formation. The high-obliquity orbit as measured by the Rossiter–McLaughlin effect (Stangret et al. 2021, see Section 5.2) suggests that the planet experienced just such a scattering event early in its history.

Future spectrally resolved emission spectra with the James Webb Space Telescope (JWST) can enable detailed analyses of the atmospheric composition and temperature–pressure profiles

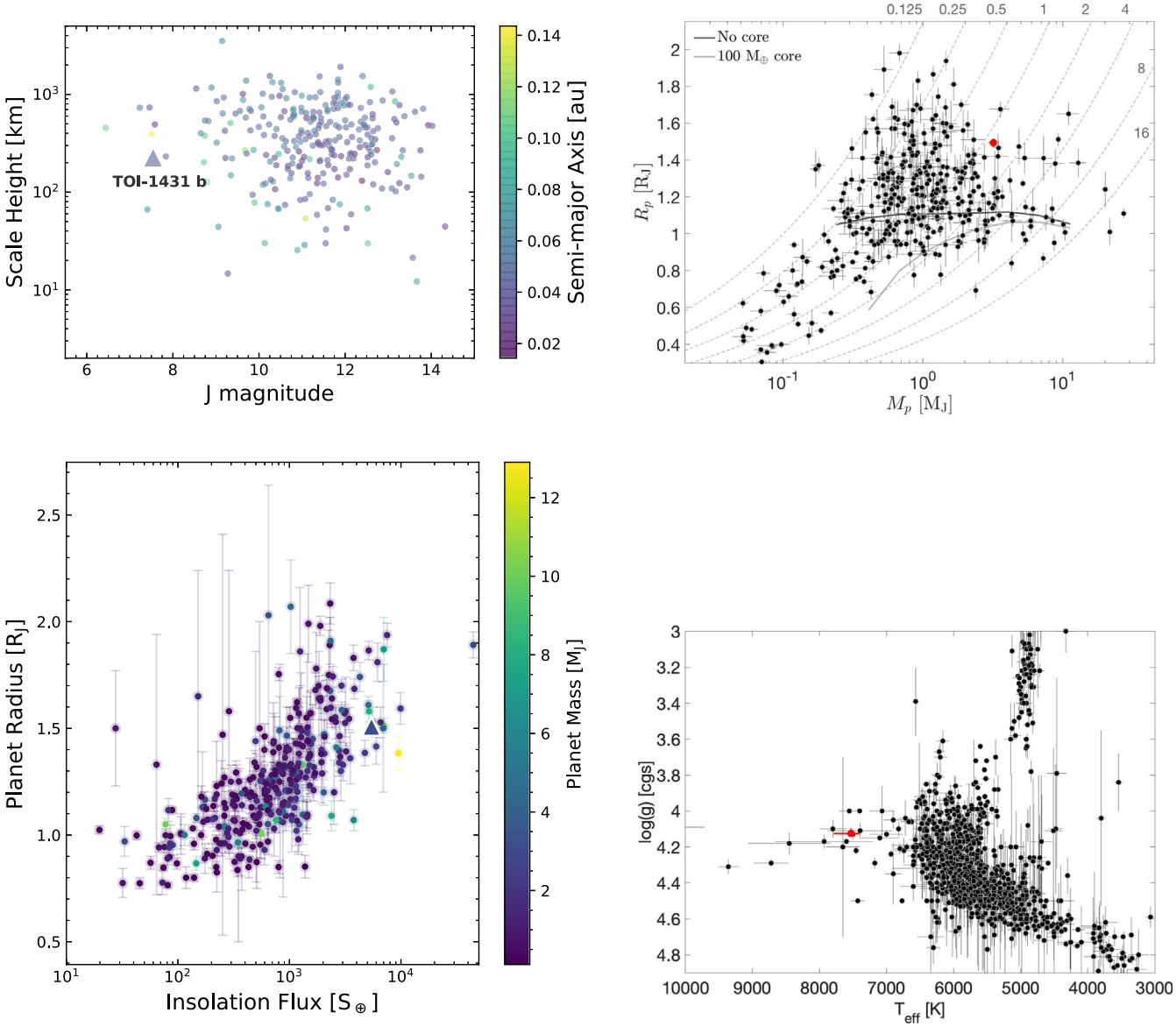

Figure 13. Comparison of TOI-1431b and its host star with other hot and ultrahot Jupiter systems. Top left: the atmospheric scale heights of hot Jupiters as a function of host star brightness in $J_{\rm mag}$. The points are colored based on the distance from the host star, with TOI-1431b plotted as a triangle. This planet transits one of the brightest stars, making it an excellent candidate for future follow-up atmospheric studies. Top right: planet mass versus radius of hot Jupiters. The red point is the location of TOI-1431b. Planets located above the dark gray solid line are predicted to have no solid core, while those plotted below the light gray solid line are predicted to have a solid core of at least 100 $M_\oplus$ (Fortney et al. 2007). The dotted lines are isodensity lines, with the density value given in the top left, in cgs units. This plot shows that TOI-1431b is moderately inflated compared to other Jovians of similar mass. Bottom left: incident stellar irradiation versus planet radius for all known Jovians and sub-Jovians that have measured masses and radii with the planet masses indicated by the color scale on the left. TOI-1431b is plotted as the colored triangle on the right and it is clear that this planet is one of the most highly irradiated planets. Bottom right: plot of stellar effective temperature versus surface gravity for planet-hosting stars. TOI-1431 is plotted as the red point and is seen to be one of the hottest (top 1%) known planet-hosting stars.

across the planet's surface, providing a full picture of the thermal energy budget for TOI-1431b.

From the derived equilibrium temperature and surface gravity of the planet and assuming an H/He atmosphere with a mean molecular mass of $\mu = 2.3$ amu, the calculated atmospheric scale height (from $H_{\rm p} = kT_{\rm eq}/(\mu g_{\rm p})$) is $H_{\rm p} = 220 \pm 30$ km. While this is not the largest scale height among the population of hot Jupiters, this planet orbits one of the brightest host stars ($J_{\rm mag} = 7.541 \pm 0.030$ and $K_{\rm mag} = 7.439 \pm 0.030$, see Figure 13), making it a potential target for future atmospheric characterization through transmission spectroscopy.

The transmission spectroscopy metric (TSM, see Kempton et al. 2018), used to assess the suitability of transmission spectroscopy observations with JWST, is ~110 for TOI-1431b. Planets with TSM values greater than 90 (for Jovians and sub-Jovians), such as for this planet, are considered suitable for these observations with JWST. However, transmission spectroscopy carried out by Stangret et al. (2021) from two HARPS-N and one EXPRES transit observations finds no absorption signatures in the planet's atmosphere, likely due to its high surface gravity. Additionally, given the detection of the phase curve and secondary eclipse in the TESS red-optical band photometry, this will be an excellent target for emission spectroscopy with JWST. In particular, phase-curve observations carried out with the Near Infrared Imager and Slitless Spectrograph (NIRISS) over wavelengths between 0.6 and

5.0 μm should provide a high-precision global temperature map of this planet's atmosphere (Parmentier & Crossfield 2018). Measurements of the abundances of molecular species as a function of longitude (chemical mapping) could also be probed through phase-resolved spectroscopic observations taken with JWST's NIRCam and NIRSpec instruments.

Previous atmospheric modeling of the extreme end-member ultrahot Jupiter KELT-9 b can serve as a guide for exploring what future intensive emission spectroscopy might reveal for TOI-1431b. The comparison is particularly apropos due to the similar planetary surface gravities of the two planets —$\log g_p = 3.30$ and 3.54 (in cgs units) for KELT-9 b and TOI-1431b, respectively. In Wong et al. (2020b), radiative transfer calculations of the dayside emission spectrum of KELT-9 b produced largely featureless spectra across the visible and near-infrared wavelength range. In contrast, model nightside emission spectra spanning 2500–3500 K showed large near-infrared absorption features due to H_2O and CO, as well as excess continuum opacity in the visible and near-infrared through $\sim$1.7 μm due to dissociated H^-; this latter spectral feature is a unique property of the hottest ultrahot Jupiters and has been studied in detail by numerous earlier theoretical works (e.g., Arcangeli et al. 2018; Lothringer et al. 2018; Parmentier et al. 2018). Measuring the detailed shape of this H^- feature can provide the abundance of H^- and the temperature–pressure profile across the nightside, which will in turn probe the effect of hydrogen dissociation on the global atmospheric dynamics and thermal energy budget.

TOI-1431b will also be a great target for detailed atmospheric characterization by the European Space Agency's Atmospheric Remote-sensing Infrared Exoplanet Large-survey (ARIEL, Tinetti et al. 2018) telescope. ARIEL will operate in the infrared with a spectral range of 1.25–7.8 μm as well as multiple narrowband photometry in the optical. As such, it will be well suited to potentially measure this planet's equilibrium chemistry, trace gases, and vertical and horizontal thermal structures, and to detect clouds and cloud composition (assuming the atmosphere is not cloud-free) through transmission and emission spectroscopy and phase-curve observations.

5. Discussion

TOI-1431b joins the growing list of $\sim$16 hot and ultrahot Jovians with measured full phase curves and secondary eclipses (e.g., see Bell et al. 2021). With dayside and nightside brightness temperatures of $T_{\rm day} = 3004 \pm 64$ K and $T_{\rm night} = 2583 \pm 63$ K, respectively, TOI-1431b is one of the hottest known exoplanets.

We have measured the mass of TOI-1431b to be $M_p = 3.12 \pm 0.18\, M_J$ from radial velocity observations obtained from the SONG, SOPHIE, FIES, NRES TLV and ELP, and EXPRES spectrographs. When combined with the planet radius of $R_p = 1.49 \pm 0.05\, R_J$, this mass gives a bulk density of $\rho_p = 1.17^{+0.18}_{-0.16}$ g cm^{-3}, similar to Jupiter (1.326 g cm^{-3}). The measured radial velocity semiamplitude of $K = 294.1 \pm 1.1$ m s^{-1} is the most precise K measurement for a planet-hosting star hotter than 6600 K. A large contributing factor for this is the unusually low projected stellar rotational velocity of $v \sin i < 10$ km s^{-1}.

Figure 13 shows a plot of the planet radius as a function of planet mass as well as a plot of planet radius as a function of stellar irradiation for all known Jovians and sub-Jovians with measured masses and radii. The radius of TOI-1431b is inflated compared to other exoplanets of similar mass as shown in Figure 13, but is not so inflated when accounting for the very high insolation flux ($5300^{+500}_{-470}\, S_\oplus$), indicating that the planet inflation is likely the result of stellar irradiation and youthful age ($0.29^{+0.32}_{-0.19}$ Gyr).

5.1. Metal-peculiar Am Star

TOI-1431b orbits a bright ($V_T \sim 8.0$ and $J \sim 7.5$) and very hot ($T_{\rm eff} \sim 7700$ K) host star. In fact, TOI-1431 is one of the hottest planet-hosting stars as shown in Figure 13. The star is also classified as being a nonmagnetic metallic-line chemically peculiar Am star (see Conti 1970; Figueras et al. 1991; Renson et al. 1991; Renson & Manfroid 2009). Am stars typically have slow rotation rates compared to typical "field" A stars of similar effective temperatures (A star $v \sin i$ range between $\sim$100 and $\sim$150 km s^{-1}; see, for example, Abt & Morrell 1995), which is certainly the case for TOI-1431 (assuming the star is not being observed nearly pole-on). The slow rotation of these stars is believed to be due to a close orbiting ($2.5 \lesssim P \lesssim 100$ days) stellar companion (at least 64% of Am stars are found to be in binary systems; see, e.g., Böhm-Vitense 2006; Carquillat & Prieur 2007) that raises tidal forces on the primary star, causing the primary to lose angular momentum and spin down (Michaud et al. 1983).

This in turn results in the onset of gravitational settling and radiative levitation due to the lack of mixing in the shallow convective envelopes of slowly rotating A stars that produces a chemical peculiarity observed as a photospheric overabundance of iron-peak elements (such as Cr, Mn, Fe, and Ni and specifically of Ba, Y, and Sr) but depleted abundances of light elements such as Ca, Sc, and Mg (e.g., see Preston 1974; Michaud et al. 1983; Charbonneau 1993; Böhm-Vitense 2006; Xiang et al. 2020).

The spectroscopic analysis of TOI-1431 from spectra collected from SONG reveals that the star has an overall metallicity slightly lower than the solar abundance ([M/H] $= -0.15 \pm 0.10$ dex) and even less so in alpha elements (such as O, Mg, Si, S, Ca, and Ti) with $[\alpha/{\rm H}] = -0.27 \pm 0.10$ dex, while analysis of the SOPHIE spectra gives a somewhat higher than solar abundance of iron ([Fe/H] $= 0.09 \pm 0.03$). This seems to suggest that the star has an overabundance of iron-group elements and an underabundance of light elements (compared with normal A stars) that is characteristic of Am stars. However, a more detailed analysis of the stellar spectra is required to confirm the Am star classification.

Another interesting feature of Am stars is the "anomalous luminosity effect", which causes deviations in the strengths of specific spectral lines from what is expected from normal main-sequence A stars at a given effective temperature (Bolton 1971). This means that, depending on the spectral lines used when fitting the stellar spectrum model, one can obtain very different values for a star's effective temperature and surface gravity, hence the overall stellar classification. This appears to be the case for TOI-1431 (especially for $\log g$); the analysis of SONG spectra gives $T_{\rm eff} = 6764 \pm 120$ K and $\log g = 2.76 \pm 0.26$ dex, the FIES spectral analysis gives $T_{\rm eff} = 6910 \pm 50$ K and $\log g = 3.29 \pm 0.10$ dex, and the SOPHIE spectral analysis gives $T_{\rm eff} = 6950 \pm 60$ K and $\log g = 4.72 \pm 0.08$ dex.

Planets orbiting main-sequence Am stars appear to be quite rare—only five that transit have been discovered to date: TOI-1431b, WASP-33 b (Collier Cameron et al. 2010b), KELT-17 b (Zhou et al. 2016; Saffe et al. 2020, 2021), KELT-19A b

(Siverd et al. 2018c), and WASP-178 b (Hellier et al. 2019)/KELT-26 b (Rodríguez Martínez et al. 2020). This raises some interesting questions. First, what is the occurrence rate of planets around Am stars? Radial velocity surveys have historically avoided hot and early type stars ($T_{\rm eff} > 6500$ K and mid-F and earlier), and instead have targeted "solar analogs" (i.e., late-F, G, and K type stars, see Cumming et al. 1999; Tinney et al. 2001; Pepe et al. 2004; Valenti & Fischer 2005; Wright et al. 2008) in the search for planets. As such, planets orbiting hot main-sequence A stars like TOI-1431 have gone nearly undiscovered, until now thanks to TESS indiscriminately surveying the sky for transiting planets orbiting bright stars. Planets have been discovered orbiting former A stars, i.e., stars that have evolved off the main sequence to become giant and subgiant stars, in radial velocity surveys targeting such stars (e.g., Johnson et al. 2006; Trifonov et al. 2014; Reffert et al. 2015; Jones et al. 2016; Luhn et al. 2019; Wittenmyer et al. 2020). Recent results from surveys of evolved stars indicate that the occurrence rate of giant planets around giant stars is ∼10% (e.g., Wittenmyer et al. 2020; Wolthoff et al., under review), indicating that giant planets are relatively common around hot stars and could also be common around Am stars as well.

If giant planet formation around A-type stars is indeed a relatively common occurrence, could the migration of a Jovian planet to a close-in orbit around its host (as presumed to be the case for TOI-1431b) play a significant role in its tidal spin-down and, as such, contribute to its nature as being an Am star? For TOI-1431b, we do not see any conclusive evidence for this given that the system does not appear to be tidally synchronized ($P_{\rm p} \simeq P_{\rm rot}$) based on the host star's rotation period of between ∼10 and ∼16 days (from spectroscopic measurements of $v \sin i$) and the planet's orbital period of ∼2.65 days. However, the one caveat is that the orientation of the stellar spin axis ($I_\star$) is unknown and the star could perhaps be spinning more rapidly if we are observing it nearly pole-on (leaving open the possibility of $P_{\rm p} \simeq P_{\rm rot}$). If indeed giant planets can contribute to the nature of their host's being an Am star, for Am stars without evidence of a stellar binary, do most or all host a hot sub-stellar or massive planetary companion? Radial velocity and transit searches targeting Am stars could resolve this question as well as provide valuable insights into the formation and evolution of Am stars, a process that is not fully understood.

5.2. Projected Spin–Orbit Angle

We attempted to measure the projected spin–orbit alignment (λ) of this system, using the planetary shadow technique (e.g., see Collier Cameron et al. 2010a; Johnson et al. 2014; Zhou et al. 2016), by acquiring in-transit HR spectroscopic observations with the FIES instrument. We observed a transit of TOI-1431b on the night of 2020 May 23 using FIES, obtaining a total of 30 exposures, each with an exposure time of 300 s and with airmass decreasing from 1.88 to 1.16 throughout the observation. The wavelength-calibrated 2D reduced spectra were extracted as outlined in Section 2.3.3. We then followed a procedure similar to that of Hoeijmakers et al. (2020) to attempt to extract the absorption line deformations during the transit of the planet. This involved first cross-correlating a continuum-normalized model template of the stellar spectrum of TOI-1431 with the telluric-corrected FIES spectra (in the stellar rest frame) to produce in-transit CCFs. The in-transit CCFs were then divided by the mean out-of-transit CCF to retrieve the Doppler shadow map.

From our analysis, the planetary shadow is not clearly detected from the FIES data, likely because of the slow rotation of the star. However, observations taken with HARPS-N and EXPRES of three transits of TOI-1431b do successfully detect the Rossiter–McLaughlin effect, revealing that the planet is on a retrograde orbit with $\lambda = -155.3^{+16.1}_{-11.3}{}^{\circ}$ (Stangret et al. 2021). The results of Stangret et al. (2021) suggest that TOI-1431b likely experienced high-eccentricity migration in the past that produced its high-obliquity orbit and then later the orbit was tidally circularized to the period of ∼2.65 days we observe today (for dissenting views of the formation of close-in gas giant planets in situ via the core-accretion process and spin–orbit misalignments due to processes unrelated to planet migration, see, e.g., Batygin et al. 2016; Hasegawa et al. 2019; Louden et al. 2021; Hjorth et al. 2021). This result follows the general pattern observed by other studies that the hottest stars tend to host planets on misaligned orbits (e.g., Winn et al. 2009; Albrecht et al. 2012; Louden et al. 2021).

6. Conclusions

We have presented the discovery of the transiting ultrahot Jupiter TOI-1431b. This planet orbits one of the hottest ($T_{\rm eff} = 7690^{+400}_{-250}$ K) and brightest ($V_T \sim 8.0$) of the known host stars with a period of just $P = 2.650237 \pm 0.000003$ days, resulting in it receiving a high amount of insolation flux and being moderately inflated. A joint analysis of the TESS light curve, ground-based light curves from MuSCAT2 and LCOGT, and radial velocities from SONG, SOPHIE, FIES, NRES, and EXPRES instruments results in a planet radius of $R_{\rm p} = 1.49 \pm 0.05\, R_{\rm J}$ ($16.7 \pm 0.6\, R_\oplus$) and a planet mass of $3.12 \pm 0.18\, M_{\rm J}$, corresponding to a bulk density of $1.17^{+0.18}_{-0.16}$ g cm^{-3}.

The planet's phase curve and secondary eclipse have been detected from the TESS photometry, providing us with the exciting opportunity to measure the planet's dayside and nightside temperatures as $T_{\rm day} = 3004 \pm 64$ K and $T_{\rm night} = 2583 \pm 63$ K, respectively, when assuming zero dayside geometric albedo. Among the population of hot/ultrahot Jupiters, TOI-1431b has the second highest measured nightside temperature and day–night heat recirculation efficiency.

It is also an excellent candidate for future follow-up observations with JWST and ARIEL to measure its transmission and emission spectra as well as to obtain a high-precision global temperature and cloud map of this planet's atmosphere. Furthermore, the discovery and characterization of planets orbiting Am stars, for which few planets have been found, provide good opportunities to probe the tidal interactions between Jovian planets and hot host stars and the potential mechanisms responsible for the creation and evolution of Am stars.

Based on observations made with the Hertzsprung SONG telescope operated on the Spanish Observatorio del Teide on the island of Tenerife by the Aarhus and Copenhagen Universities and by the Instituto de Astrofísica de Canarias.

Funding for the Stellar Astrophysics Centre is provided by The Danish National Research Foundation (grant agreement no.: DNRF106).

Based on observations made with the Nordic Optical Telescope, operated by the Nordic Optical Telescope Scientific Association at the Observatorio del Roque de los Muchachos,

La Palma, Spain, of the Instituto de Astrofisica de Canarias under programs 59-210, 59-503, and 61-804.

Based on observations collected with the SOPHIE spectrograph on the 1.93 m telescope at the Observatoire de Haute-Provence (CNRS), France.

This article is based on observations made with the MuSCAT2 instrument, developed by ABC, at Telescopio Carlos Sánchez operated on the island of Tenerife by the IAC in the Spanish Observatorio del Teide.

This work makes use of observations from the LCOGT network. LCOGT telescope time was granted by NOIRLab through the Mid-Scale Innovations Program (MSIP). MSIP is funded by NSF.

B.A. is supported by Australian Research Council Discovery Grant DP180100972. The SONG telescope network is partially supported by the Australian Research Council Linkage, Infrastructure, Equipment and Facilities grant LE190100036.

V.A. was supported by a research grant (00028173) from VILLUM FONDEN.

I.W. is supported by a Heising–Simons 51 Pegasi b postdoctoral fellowship.

Funding for the TESS mission is provided by NASA's Science Mission directorate. We acknowledge the use of public TESS Alert data from pipelines at the TESS Science Office and at the TESS Science Processing Operations Center. This research has made use of the Exoplanet Follow-up Observation Program website, which is operated by the California Institute of Technology, under contract with the National Aeronautics and Space Administration under the Exoplanet Exploration Program. Resources supporting this work were provided by the NASA High-End Computing (HEC) Program through the NASA Advanced Supercomputing (NAS) Division at Ames Research Center for the production of the SPOC data products. This paper includes data collected by the TESS mission, which are publicly available from the Mikulski Archive for Space Telescopes (MAST).

T.D. acknowledges support from MIT's Kavli Institute as a Kavli postdoctoral fellow.

M.Y. and H.V.S. acknowledge the support by the research fund of Ankara University (BAP) through the project 18A0759001.

This work was supported by Fundação para a Ciência e a Tecnologia (FCT) and Fundo Europeu de Desenvolvimento Regional (FEDER) via COMPETE2020 through the research grants UIDB/04434/2020, UIDP/04434/2020, PTDC/FIS-AST/32113/2017 and POCI-01-0145-FEDER-032113, PTDC/FIS-AST/28953/2017 and POCI-01-0145-FEDER-028953.

O.D.S.D. is supported in the form of work contract (DL 57/2016/CP1364/CT0004) funded by FCT.

This work was supported by FCT—Fundação para a Ciência e a Tecnologia through national funds and by FEDER through COMPETE2020—Programa Operacional Competitividade e Internacionalização by these grants: UID/FIS/04434/2019; UIDB/04434/2020; UIDP/04434/2020; PTDC/FIS-AST/32113/2017 and POCI-01-0145-FEDER-032113; PTDC/FIS-AST/28953/2017 and POCI-01-0145-FEDER-028953; PTDC/FIS-AST/28987/2017 and POCI-01-0145-FEDER-028987.

S.H. acknowledges CNES funding through the grant 837319

G.H. and I.B. received funding from the French Programme National de Planétologie (PNP) of CNRS (INSU).

This work is partly supported by JSPS KAKENHI Grant Nos. JP18H01265 and JP18H05439, and JST PRESTO grant No. JPMJPR1775, and a University Research Support Grant from the National Astronomical Observatory of Japan (NAOJ).

M.N.G. acknowledges support from MIT's Kavli Institute as a Juan Carlos Torres Fellow.

T.D.K. acknowledges support from the 51 Pegasi b Fellowship in Planetary Astronomy sponsored by the Heising–Simons Foundation.

D.R.L. is supported by an appointment to the NASA Postdoctoral Program at NASA Goddard Space Flight Center, administered by Universities Space Research Association under contract with NASA.

Facilities: TESS, SONG, SOPHIE, NRES ELP, NRES TLV, FIES, EXPRES, LCOGT, MuSCAT2, MASCARA.

Software: AstroImageJ (Collins et al. 2017), TAPIR (Jensen 2013), `Allesfitter` (Günther & Daylan 2019, 2021), EXOFASTv2 (Eastman et al. 2013, 2019; Eastman 2017), Astropy (Astropy Collaboration et al. 2018), Matplotlib (Hunter 2007), Wotan (Hippke et al. 2019).

Appendix

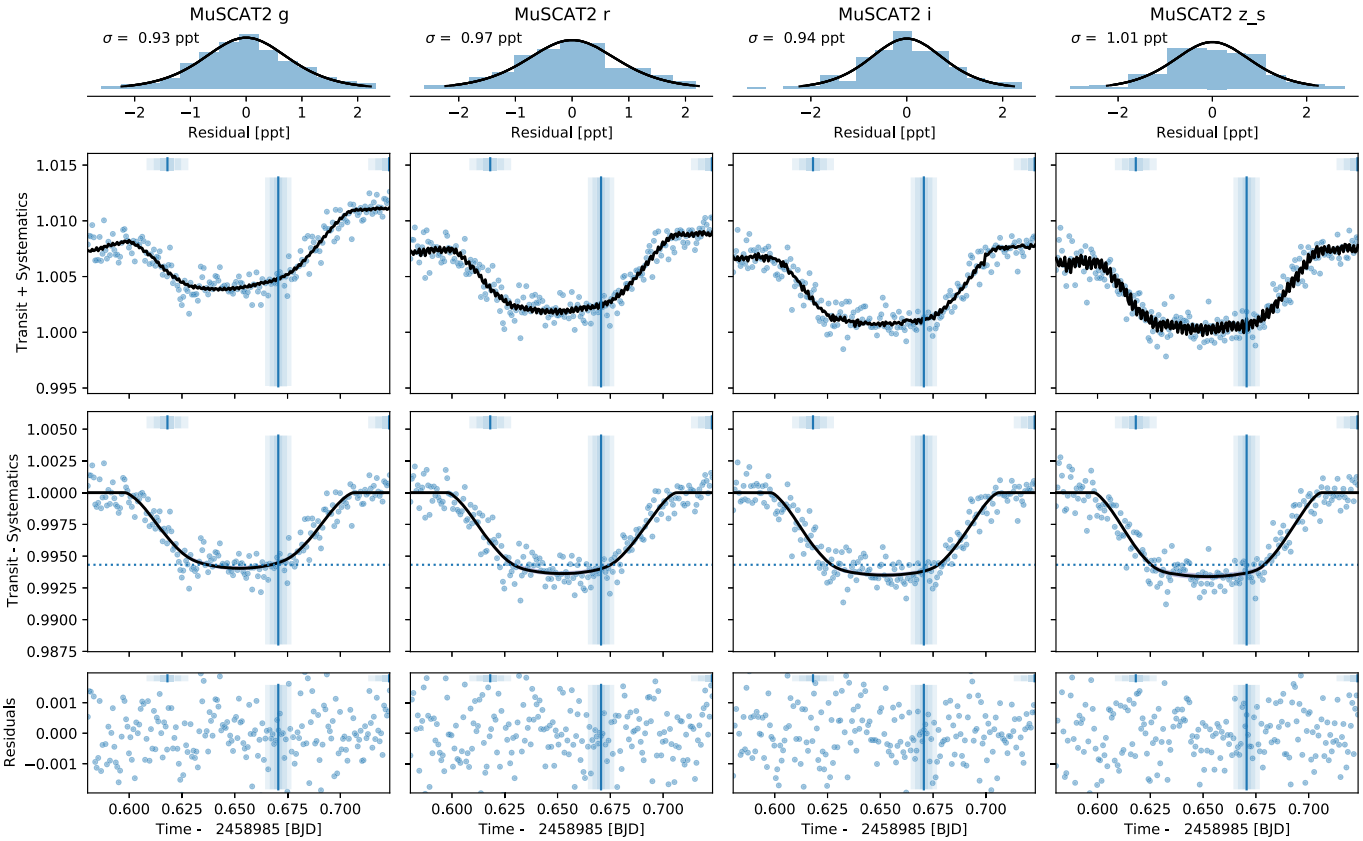

Figure 14. A transit observed on 2020 May 16 by MuSCAT2 using simultaneous multicolor photometry in g', r', i', and z_s bands. The top panel shows the distribution of residuals to the fit of the light curve in each band. The second panel from the top shows the fit to the transit plus systematics. The third panel shows the fit to the transit with the systematics removed. The three blue vertical bars in the second, third, and fourth panels represent the predicted ingress, mid-transit, and egress times along with their 1σ uncertainties based on the ephemeris used at the time. The horizontal dotted blue lines in the third panel show the predicted transit depth. The bottom panel shows the resulting residuals to the fit of the light curves.

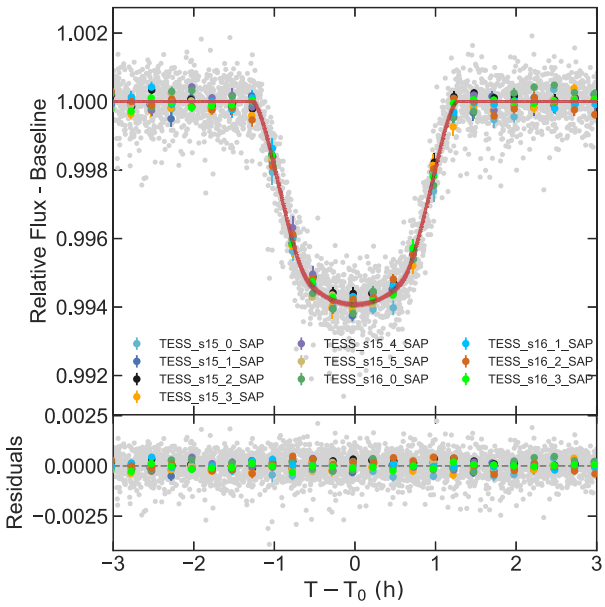

Figure 15. Phase-folded and detrended light curve of TOI-1431 from the simultaneous hybrid cubic spline detrending model using the SAP data. The colored points represent the individual phased light-curve segments across Sectors 15 and 16 that have been binned at a cadence of 15 minutes. The red solid lines are 20 light-curve models drawn from the posteriors of the nested sampling analysis in `Allesfitter`.

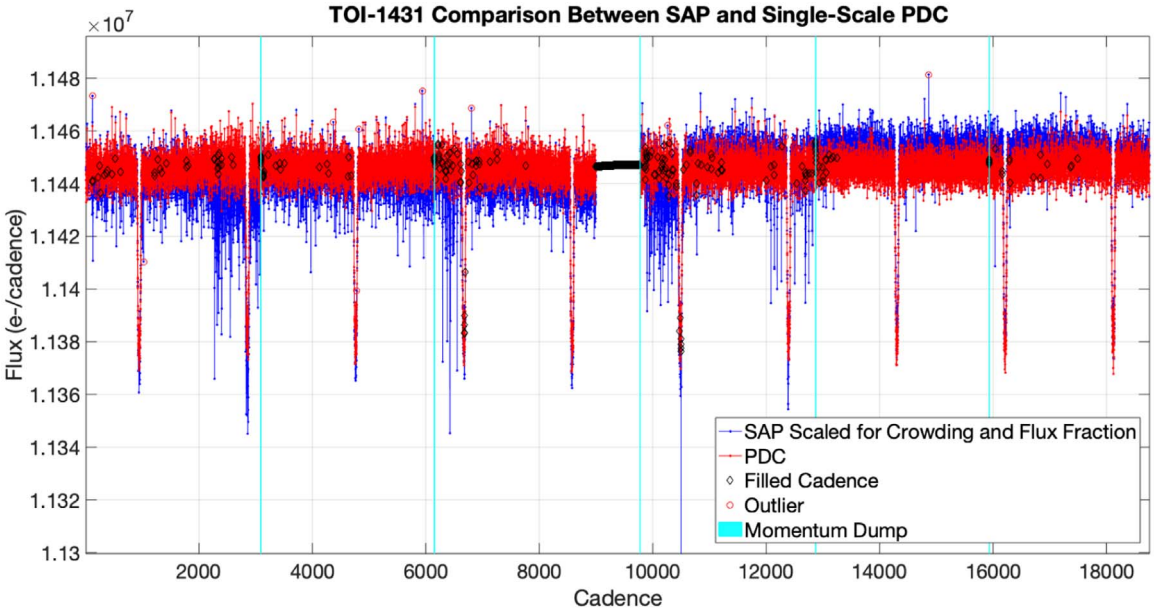

Figure 16. TESS Sector 15 photometry of TOI-1431 from the SAP (blue points) and single-scale MAP PDC (red points) light curves. The SAP light curve shows "whisker"-like flux dips that are caused by brief spacecraft pointing excursions, some of which overlap with the transit events. The correction applied to the single-scale MAP PDC light curve from the use of the cotrending basis vectors has removed these features.

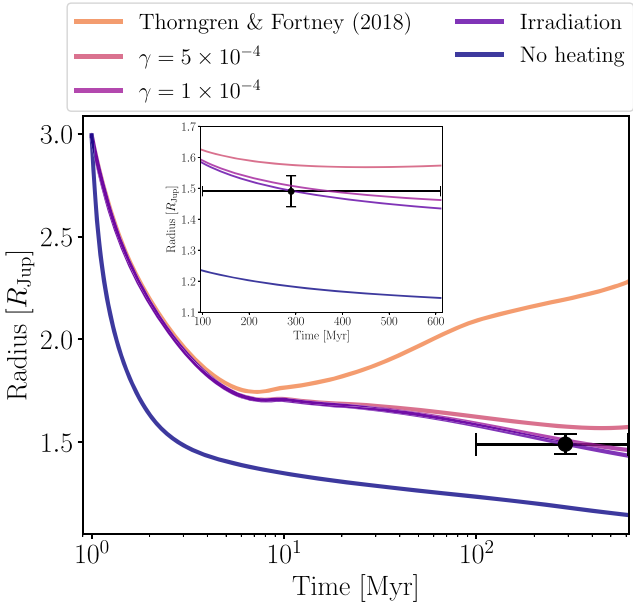

Figure 17. Radius evolution of TOI-1431b for various assumptions about the presence of irradiation and deep deposited heating. The curve labeled Thorngren & Fortney (2018) includes irradiation and applies deposited heating in the deep interior with a strength that varies with equilibrium temperature, as in Equation (34) of Thorngren & Fortney (2018). The models labeled $\gamma = 5 \times 10^{-4}$ and $\gamma = 1 \times 10^{-4}$ respectively assume that 0.05% and 0.01% of the incident stellar power is converted to heat deposited deep in the planetary interior and include irradiation. The model labeled "irradiation" considers only irradiation with no deposited heating, and the model labeled "no heating" does not include irradiation or deposited heating. Evolution models are conducted with MESA (Paxton et al. 2011, 2013, 2015, 2018, 2019) using the model setup described in Komacek et al. (2020) and stellar evolution tracks from Choi et al. (2016) and Dotter (2016). The present-day radius of TOI-1431b can be fit by planetary evolution models including only irradiation slowing cooling, but a small amount of deep deposited heating corresponding to <0.05% of the incident stellar power converted to heat is allowed.

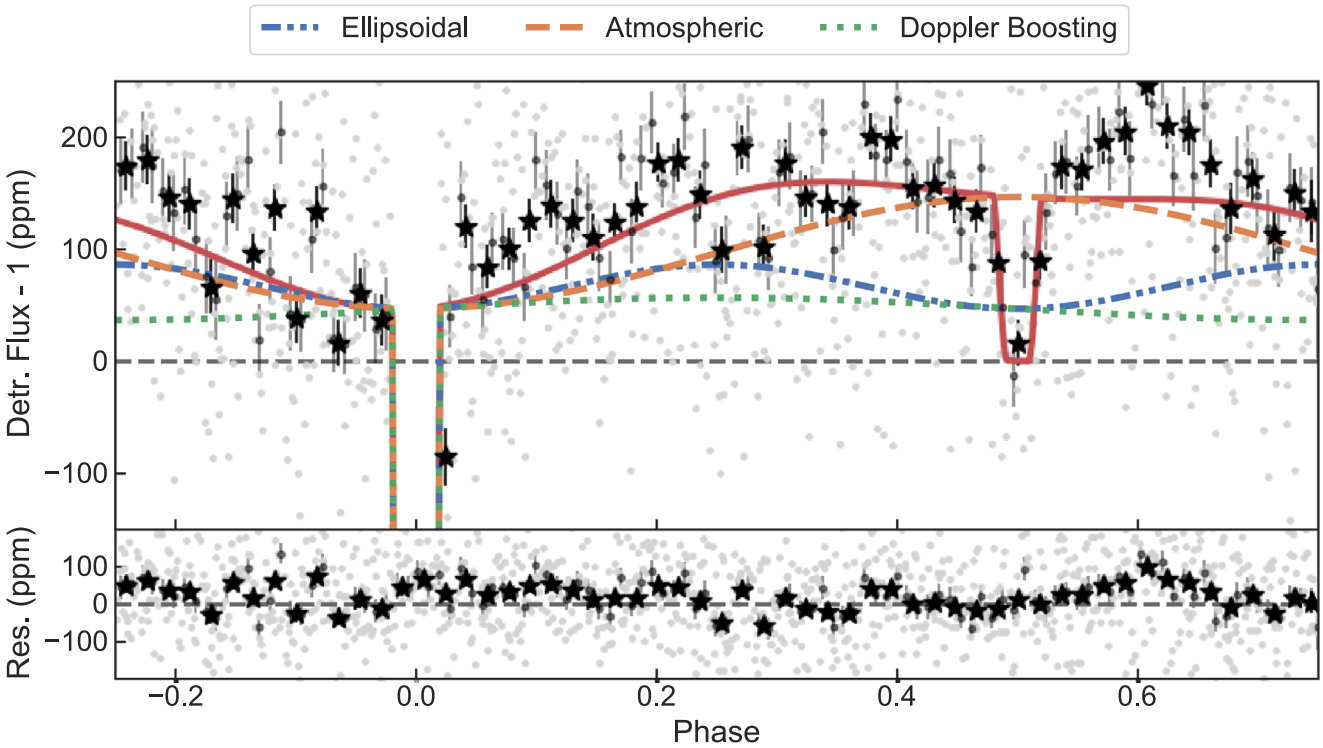

Figure 18. The phase-folded TESS SAP light curve for TOI-1431b, zoomed in to show the phase curve and secondary eclipse, similar to Figure 11.

Table 3
A Summary of the Ground-based Transit Follow-up Observations Taken of TOI-1431

Telescope	Camera	Filter	UT Date	Coverage	Precision (ppt)	Joint Fit	Comments
CDK14	STXL-6303E	z'	2019-12-24	Full	2.62	Yes	Minimal systematics
CDK14	STXL-6303E	g'	2019-12-24	Full	2.32	Yes	Minimal systematics
TCS	MuSCAT2	g'	2020-05-16	Full	0.93	Yes	Minimal systematics
TCS	MuSCAT2	r'	2020-05-16	Full	0.97	Yes	Minimal systematics
TCS	MuSCAT2	i'	2020-05-16	Full	0.94	Yes	Minimal systematics
TCS	MuSCAT2	z_s	2020-05-16	Full	1.01	Yes	Minimal systematics
TCS	MuSCAT2	g'	2020-05-23	Full	1.23	No	Limited pre-ingress data and systematics
TCS	MuSCAT2	r'	2020-05-23	Full	1.07	No	Limited pre-ingress data and systematics
TCS	MuSCAT2	i'	2020-05-23	Full	1.08	No	Limited pre-ingress data and systematics
TCS	MuSCAT2	z_s	2020-05-23	Full	1.09	No	Limited pre-ingress data and systematics
AUKR	ALTA U47	z'	2020-06-16	Full	3.00	Yes	Some systematics
LCOGT-McD	Sinistro	PANSTARRS Y	2020-07-13	Ingress	0.48	No	Ingress only
SCT	ST7XME	TESS band	2020-08-08	Full	1.49	Yes	Minimal systematics
ULMT	STX 16803	i'	2020-09-20	Full	1.51	Yes	Some systematics
ULMT	STX 16803	i'	2020-09-28	Full	3.41	No	Significant systematics
LCOGT-McD	Sinistro	PANSTARRS Y	2020-10-14	Full	1.18	Yes	Minimal systematics

Table 4
Radial Velocity Measurements

Date[a] BJD − 2,400,000	RV[b] (m s^{-1})	σ_{RV} (m s^{-1})	Instrument
58,805.564199	−25,696.6	14.5	ELP
58,806.565002	−25,761.0	15.3	ELP
58,807.566340	−25,346.6	13.3	ELP
58,808.570467	−25,830.7	29.9	ELP
58,814.663425	−25,557.9	26.2	ELP
58,815.307593	9.2	14.2	FIES
58,818.618086	−25,457.5	18.0	ELP
58,836.224800	−25,039.0	7.0	SOPHIE
58,838.252200	−25,441.0	7.0	SOPHIE
58,840.399100	−25,532.0	45.0	SOPHIE
58,841.235500	−25,222.0	7.0	SOPHIE
58,841.352100	−25,152.0	6.0	SOPHIE
58,859.232100	−25,528.0	7.0	SOPHIE
58,860.267700	−24,987.0	6.0	SOPHIE
58,861.259600	−25,374.0	6.0	SOPHIE
58,914.768952	−25,465.4	53.1	SONG
58,919.763375	−25,434.9	81.7	SONG
58,921.764647	−24,969.6	74.1	SONG
58,942.562272	−25,283.8	19.2	TLV
58,943.567282	−25,788.4	15.4	TLV
58,948.564452	−25,514.9	16.4	TLV
58,952.584719	−25,528.9	16.3	TLV
58,955.532830	−25,299.7	28.7	TLV
58,956.668739	−25,303.1	139.4	SONG
58,961.645589	−25,067.3	56.1	SONG
58,965.721756	−25,219.0	44.1	SONG
58,980.495174	−25,900.9	19.9	TLV
58,982.464359	−25,256.1	27.5	TLV
58,983.637401	−25,477.9	64.2	SONG
58,987.442635	−25,265.9	22.1	TLV
58,988.470752	−25,659.4	27.9	TLV
58,988.619270	−25,374.0	26.6	SONG
58,989.466532	−25,588.9	42.2	TLV
58,990.449283	−25,278.6	20.1	TLV
58,990.567802	−24.1	7.9	FIES
58,991.456242	−25,896.5	26.1	TLV
58,991.562807	−581.4	15.6	FIES
58,991.594498	−565.9	12.9	FIES
58,991.642527	−25,435.4	18.0	SONG
58,991.698593	−565.4	11.0	FIES
58,992.606914	−69.5	12.5	FIES
58,992.615274	−75.2	18.9	FIES
58,993.658735	−318.3	11.6	FIES
58,993.662679	−339.5	15.6	FIES
58,993.666687	−314.2	14.1	FIES
58,993.670878	−329.4	18.3	FIES
58,993.674862	−315.8	11.2	FIES
58,993.678937	−333.8	13.4	FIES
58,993.686045	−334.8	9.8	FIES
58,993.690092	−329.0	13.9	FIES
58,993.694137	−337.2	13.8	FIES
58,993.698146	−345.5	9.7	FIES
58,994.571980	−500.4	9.3	FIES
58,994.621049	−471.6	8.0	FIES
58,994.704411	−429.4	11.7	FIES
58,995.443468	−25,324.0	28.7	TLV
58,995.570851	15.5	11.5	FIES
58,995.620876	13.7	7.2	FIES
58,995.703476	0.0	11.9	FIES
58,996.502720	−25,732.7	26.1	TLV
58,997.422153	−25,702.1	38.1	TLV
58,998.422132	−25,287.5	23.5	TLV
58,999.424288	−25,873.9	19.0	TLV

Table 4
(Continued)

Date[a] BJD − 2,400,000	RV[b] (m s^{-1})	σ_{RV} (m s^{-1})	Instrument
58,999.624293	−25,458.0	76.4	SONG
59,001.471298	−25,606.2	20.1	TLV
59,001.641856	−25,224.1	28.8	SONG
59,002.428683	−25,802.8	21.2	TLV
59,002.787631	−55.3	2.5	EXPRES
59,003.954076	167.7	1.8	EXPRES
59,004.452546	−25,721.2	16.9	TLV
59,004.602433	−25,375.3	24.6	SONG
59,004.953876	−279.8	2.0	EXPRES
59,005.450710	−25,560.8	18.8	TLV
59,006.382260	−25,320.8	19.6	TLV
59,007.421885	−25,873.3	17.2	TLV
59,007.604415	−25,444.7	39.9	SONG
59,008.456417	−25,235.3	34.6	TLV
59,009.487869	−25,570.9	18.7	TLV
59,009.566599	−25,187.8	24.2	SONG
59,010.502769	−25,751.8	19.5	TLV
59,010.624528	−25,295.0	24.9	SONG
59,012.426456	−25,777.6	16.5	TLV
59,012.640398	−25,419.6	29.3	SONG
59,012.955625	−271.6	1.9	EXPRES
59,018.520808	−447.3	17.6	FIES
59,018.597262	−406.4	15.7	FIES
59,018.693433	−330.5	8.5	FIES
59,019.513133	34.7	8.4	FIES
59,019.594250	2.8	7.5	FIES
59,019.694408	−25.8	9.3	FIES
59,020.514030	−516.7	10.5	FIES
59,020.590422	−546.9	9.0	FIES
59,020.688977	−552.9	12.6	FIES
59,023.610494	−25,418.5	21.3	SONG
59,027.569361	−24,874.0	24.4	SONG
59,029.510059	−25,065.6	20.3	SONG
59,033.957319	−287.7	2.2	EXPRES
59,059.915400	−36.2	2.1	EXPRES
59,059.919605	−44.0	2.0	EXPRES
59,059.923762	−38.9	2.0	EXPRES
59,059.927997	−45.9	2.2	EXPRES
59,059.932407	−51.7	2.2	EXPRES
59,059.936606	−50.3	2.3	EXPRES
59,059.940835	−50.7	2.2	EXPRES
59,059.945055	−58.2	2.1	EXPRES
59,059.949247	−59.5	1.9	EXPRES
59,059.953490	−62.4	2.3	EXPRES

Notes.
[a] The dates for each observation are reported as BJD at the UTC time at the midpoint of the exposure.
[b] FIES and EXPRES radial velocities are given at an arbitrary zero-point.

(This table is available in machine-readable form.)

ORCID iDs

Brett C. Addison https://orcid.org/0000-0003-3216-0626
Emil Knudstrup https://orcid.org/0000-0001-7880-594X
Ian Wong https://orcid.org/0000-0001-9665-8429
Ignas Snellen https://orcid.org/0000-0003-1624-3667
Simon Albrecht https://orcid.org/0000-0003-1762-8235
Aaron Bello-Arufe https://orcid.org/0000-0003-3355-1223
Jose-Manuel Almenara https://orcid.org/0000-0003-3208-9815

Sergio Hoyer https://orcid.org/0000-0003-3477-2466
N. C. Santos https://orcid.org/0000-0003-4422-2919
Grzegorz Nowak https://orcid.org/0000-0002-7031-7754
Rafael Luque https://orcid.org/0000-0002-4671-2957
Monika Stangret https://orcid.org/0000-0002-1812-8024
Enric Palle https://orcid.org/0000-0003-0987-1593
René Tronsgaard https://orcid.org/0000-0003-1001-0707
Victoria Antoci https://orcid.org/0000-0002-0865-3650
Lars A. Buchhave https://orcid.org/0000-0003-1605-5666
Maximilian N. Günther https://orcid.org/0000-0002-3164-9086
Tansu Daylan https://orcid.org/0000-0002-6939-9211
Felipe Murgas https://orcid.org/0000-0001-9087-1245
Hannu Parviainen https://orcid.org/0000-0001-5519-1391
Emma Esparza-Borges https://orcid.org/0000-0002-2341-3233
Nicolas Crouzet https://orcid.org/0000-0001-7866-8738
Norio Narita https://orcid.org/0000-0001-8511-2981
Akihiko Fukui https://orcid.org/0000-0002-4909-5763
Kiyoe Kawauchi https://orcid.org/0000-0003-1205-5108
Noriharu Watanabe https://orcid.org/0000-0002-7522-8195
Markus Rabus https://orcid.org/0000-0003-2935-7196
Marshall C. Johnson https://orcid.org/0000-0002-5099-8185
Gilles P. P. L. Otten https://orcid.org/0000-0002-6717-1977
Geert Jan Talens https://orcid.org/0000-0003-4787-2335
Samuel H. C. Cabot https://orcid.org/0000-0001-9749-6150
Debra A. Fischer https://orcid.org/0000-0003-2221-0861
Frank Grundahl https://orcid.org/0000-0002-8736-1639
Mads Fredslund Andersen https://orcid.org/0000-0002-9194-8520
Pere Pallé https://orcid.org/0000-0003-3803-4823
Avi Shporer https://orcid.org/0000-0002-1836-3120
David R. Ciardi https://orcid.org/0000-0002-5741-3047
Jake T. Clark https://orcid.org/0000-0003-3964-4658
Robert A. Wittenmyer https://orcid.org/0000-0001-9957-9304
Jonathan Horner https://orcid.org/0000-0002-1160-7970
Karen A. Collins https://orcid.org/0000-0001-6588-9574
Eric L. N. Jensen https://orcid.org/0000-0002-4625-7333
John F. Kielkopf https://orcid.org/0000-0003-0497-2651
Richard P. Schwarz https://orcid.org/0000-0001-8227-1020
Mesut Yilmaz https://orcid.org/0000-0002-3276-0704
Hakan Volkan Senavci https://orcid.org/0000-0002-8961-277X
Daniel Harbeck https://orcid.org/0000-0002-8590-007X
Thaddeus D. Komacek https://orcid.org/0000-0002-9258-5311
Songhu Wang https://orcid.org/0000-0002-7846-6981
Jason D. Eastman https://orcid.org/0000-0003-3773-5142
Keivan G. Stassun https://orcid.org/0000-0002-3481-9052
David W. Latham https://orcid.org/0000-0001-9911-7388
Roland Vanderspek https://orcid.org/0000-0001-6763-6562
Sara Seager https://orcid.org/0000-0002-6892-6948
Joshua N. Winn https://orcid.org/0000-0002-4265-047X
Jon M. Jenkins https://orcid.org/0000-0002-4715-9460
Dana R. Louie https://orcid.org/0000-0002-2457-272X
Luke G. Bouma https://orcid.org/0000-0002-0514-5538
Joseph D. Twicken https://orcid.org/0000-0002-6778-7552
Alan M. Levine https://orcid.org/0000-0001-8172-0453
Brian McLean https://orcid.org/0000-0002-8058-643X

References

Abt, H. A., & Morrell, N. I. 1995, ApJS, 99, 135
Addison, B. C., Tinney, C. G., Wright, D. J., et al. 2013, ApJL, 774, L9
Addison, B. C., Wright, D. J., Nicholson, B. A., et al. 2021, MNRAS, 502, 3704
Albrecht, S., Winn, J. N., Butler, R. P., et al. 2012, ApJ, 744, 189
Alibert, Y., Mordasini, C., Benz, W., & Winisdoerffer, C. 2005, A&A, 434, 343
Andersen, M. F., Grundahl, F., Christensen-Dalsgaard, J., et al. 2014, RMxAA, 45, 83
Anderson, D. R., Temple, L. Y., Nielsen, L. D., et al. 2018, arXiv:1809.04897
Antoci, V., Handler, G., Grundahl, F., et al. 2013, MNRAS, 435, 1563
Arcangeli, J., Désert, J.-M., Line, M. R., et al. 2018, ApJL, 855, L30
Asplund, M., Grevesse, N., Sauval, A. J., & Scott, P. 2009, ARA&A, 47, 481
Astropy Collaboration, Price-Whelan, A. M., Sipőcz, B. M., et al. 2018, AJ, 156, 123
Batygin, K., Bodenheimer, P. H., & Laughlin, G. P. 2016, ApJ, 829, 114
Beaugé, C., & Nesvorný, D. 2012, ApJ, 751, 119
Bell, T. J., & Cowan, N. B. 2018, ApJL, 857, L20
Bell, T. J., Dang, L., Cowan, N. B., et al. 2021, MNRAS, 504, 3316
Bergmann, C., Jones, M. I., Zhao, J., et al. 2021, PASA, 38, 19
Blackman, R. T., Fischer, D. A., Jurgenson, C. A., et al. 2020, AJ, 159, 238
Blanco-Cuaresma, S. 2019, MNRAS, 486, 2075
Blanco-Cuaresma, S., Soubiran, C., Heiter, U., & Jofré, P. 2014, A&A, 569, A111
Böhm-Vitense, E. 2006, PASP, 118, 419
Böhm-Vitense, E. 2007, AJ, 133, 1903
Bolton, C. T. 1971, A&A, 14, 233
Borucki, W. J., Koch, D., Basri, G., et al. 2010, Sci, 327, 977
Bouchy, F., Hébrard, G., Udry, S., et al. 2009, A&A, 505, 853
Bowler, B. P., Johnson, J. A., Marcy, G. W., et al. 2010, ApJ, 709, 396
Brahm, R., Jordán, A., & Espinoza, N. 2017, PASP, 129, 034002
Brahm, R., Nielsen, L. D., Wittenmyer, R. A., et al. 2020, AJ, 160, 235
Brewer, J. M., Fischer, D. A., Blackman, R. T., et al. 2020, AJ, 160, 67
Brown, T. M., Baliber, N., Bianco, F. B., et al. 2013, PASP, 125, 1031
Bryson, S., Kunimoto, M., Kopparapu, R. K., et al. 2021, AJ, 161, 36
Buchhave, L. A., Bizzarro, M., Latham, D. W., et al. 2014, Natur, 509, 593
Buchhave, L. A., Bakos, G. Á., Hartman, J. D., et al. 2010, ApJ, 720, 1118
Buchhave, L. A., Latham, D. W., Johansen, A., et al. 2012, Natur, 486, 375
Butler, R. P., Marcy, G. W., Fischer, D. A., et al. 1999, ApJ, 526, 916
Butler, R. P., Marcy, G. W., Vogt, S. S., & Apps, K. 1998, PASP, 110, 1389
Cañas, C. I., Wang, S., Mahadevan, S., et al. 2019, ApJL, 870, L17
Carquillat, J. M., & Prieur, J. L. 2007, MNRAS, 380, 1064
Castelli, F., & Kurucz, R. L. 2003, in IAU Symp. 210, Modelling of Stellar Atmospheres, ed. N. Piskunov, W. W. Weiss, & D. F. Gray (Cambridge: Cambridge Univ. Press), A20
Charbonneau, P. 1993, in ASP Conf. Ser. 44, IAU Coll. 138: Peculiar versus Normal Phenomena in A-type and Related Stars, ed. M. M. Dworetsky, F. Castelli, & R. Faraggiana (San Francisco, CA: ASP), 474
Chatterjee, S., Ford, E. B., Matsumura, S., & Rasio, F. A. 2008, ApJ, 686, 580
Choi, J., Dotter, A., Conroy, C., et al. 2016, ApJ, 823, 102
Claret, A. 2017, A&A, 600, A30
Cochran, W. D., Hatzes, A. P., Butler, R. P., & Marcy, G. W. 1997, ApJ, 483, 457
Collier Cameron, A., Bruce, V. A., Miller, G. R. M., Triaud, A. H. M. J., & Queloz, D. 2010a, MNRAS, 403, 151
Collier Cameron, A., Guenther, E., Smalley, B., et al. 2010b, MNRAS, 407, 507
Collins, K. A., Kielkopf, J. F., Stassun, K. G., & Hessman, F. V. 2017, AJ, 153, 77
Conti, P. S. 1970, PASP, 82, 781
Courcol, B., Bouchy, F., Pepe, F., et al. 2015, A&A, 581, A38
Cowan, N. B., & Agol, E. 2011, ApJ, 729, 54
Cumming, A., Marcy, G. W., & Butler, R. P. 1999, ApJ, 526, 890
Cutri, R. M., Skrutskie, M. F., van Dyk, S., et al. 2003, yCat, 2246, 0
Cutri, R. M., Skrutskie, M. F., van Dyk, S., et al. 2013, Explanatory Supplement to the AllWISE Data Release Products
Davis, A. B., Wang, S., Jones, M., et al. 2020, AJ, 160, 229
Daylan, T., Günther, M. N., Mikal-Evans, T., et al. 2021, AJ, 161, 131
Djupvik, A. A., & Andersen, J. 2010, ASSP, 14, 211
Dorn, C., Harrison, J. H. D., Bonsor, A., & Hands, T. O. 2019, MNRAS, 484, 712
Dorval, P., Talens, G. J. J., Otten, G. P. P. L., et al. 2020, A&A, 635, A60
Dotter, A. 2016, ApJS, 222, 8

Eastman, J. 2017, EXOFASTv2: Generalized publication-quality exoplanet modeling code, Astrophysics Source Code Library, http://ascl.net/1710.003
Eastman, J., Gaudi, B. S., & Agol, E. 2013, PASP, 125, 83
Eastman, J. D., Rodriguez, J. E., Agol, E., et al. 2019, arXiv:1907.09480
Endl, M., Cochran, W. D., Wittenmyer, R. A., & Boss, A. P. 2008, ApJ, 673, 1165
Figueras, F., Torra, J., & Jordi, C. 1991, A&AS, 87, 319
Fortney, J. J., Marley, M. S., & Barnes, J. W. 2007, ApJ, 659, 1661
Frandsen, S., & Lindberg, B. 1999, in Astrophysics with the NOT, ed. H. Karttunen & V. Piirola (Piikkio: University of Turku, Tuorla Observatory), 71
Fredslund Andersen, M., Handberg, R., Weiss, E., et al. 2019, PASP, 131, 045003
Gaia Collaboration, Brown, A. G. A., Vallenari, A., et al. 2018a, A&A, 616, A1
Gaudi, B. S., Stassun, K. G., Collins, K. A., et al. 2017, Natur, 546, 514
Gilbert, E. A., Barclay, T., Schlieder, J. E., et al. 2020, AJ, 160, 116
Ginzburg, S., & Sari, R. 2015, ApJ, 803, 111
Gray, R. O., & Corbally, C. J. 1994, AJ, 107, 742
Grundahl, F., Fredslund Andersen, M., Christensen-Dalsgaard, J., et al. 2017, ApJ, 836, 142
Guenther, E. W., Barragán, O., Dai, F., et al. 2017, A&A, 608, A93
Guerrero, N. M., Seager, S., Huang, C. X., et al. 2021, ApJS, 254, 39
Günther, M. N., & Daylan, T. 2019, Allesfitter: Flexible Star and Exoplanet Inference From Photometry and Radial Velocity, Astrophysics Source Code Library, http://ascl.net/1903.003
Günther, M. N., & Daylan, T. 2021, ApJS, 254, 13
Günther, M. N., Pozuelos, F. J., Dittmann, J. A., et al. 2019, NatAs, 3, 1099
Gustafsson, B., Edvardsson, B., Eriksson, K., et al. 2008, A&A, 486, 951
Hasegawa, Y., Yu, T. Y. M., & Hansen, B. M. S. 2019, A&A, 629, L1
Heiter, U., Lind, K., Asplund, M., et al. 2015, PhyS, 90, 054010
Hellier, C., Anderson, D. R., Barkaoui, K., et al. 2019, MNRAS, 490, 1479
Henry, G. W., Marcy, G. W., Butler, R. P., & Vogt, S. S. 2000, ApJL, 529, L41
Hippke, M., David, T. J., Mulders, G. D., & Heller, R. 2019, AJ, 158, 143
Hirano, T., Narita, N., Sato, B., et al. 2011, PASJ, 63, L57
Hjorth, M., Albrecht, S., Hirano, T., et al. 2021, PNAS, 118, 2017418118
Hoeijmakers, H. J., Seidel, J. V., Pino, L., et al. 2020, A&A, 641, A123
Høg, E., Fabricius, C., Makarov, V. V., et al. 2000, A&A, 355, L27
Horner, J., Kane, S. R., Marshall, J. P., et al. 2020, PASP, 132, 102001
Hsu, D. C., Ford, E. B., Ragozzine, D., & Ashby, K. 2019, AJ, 158, 109
Huang, C. X., Burt, J., Vanderburg, A., et al. 2018, ApJL, 868, L39
Hunter, J. D. 2007, CSE, 9, 90
Husser, T. O., Wende-von Berg, S., Dreizler, S., et al. 2013, A&A, 553, A6
Ida, S., & Lin, D. N. C. 2005, ApJ, 626, 1045
Jenkins, J. M., Twicken, J. D., McCauliff, S., et al. 2016, Proc. SPIE, 9913, 99133E
Jensen, E. 2013, Tapir: A web interface for transit/eclipse observability, Astrophysics Source Code Library, http://ascl.net/1306.007
Johnson, J. A., Marcy, G. W., Fischer, D. A., et al. 2006, ApJ, 652, 1724
Johnson, M. C., Cochran, W. D., Albrecht, S., et al. 2014, ApJ, 790, 30
Jones, H. R. A., Butler, R. P., Tinney, C. G., et al. 2006, MNRAS, 369, 249
Jones, M. I., Brahm, R., Espinoza, N., et al. 2019, A&A, 625, A16
Jones, M. I., Jenkins, J. S., Brahm, R., et al. 2016, A&A, 590, A38
Jordán, A., Brahm, R., Espinoza, N., et al. 2020, AJ, 159, 145
Jurgenson, C., Fischer, D., McCracken, T., et al. 2016, Proc. SPIE, 9908, 99086T
Kempton, E. M. R., Bean, J. L., Louie, D. R., et al. 2018, PASP, 130, 114401
Komacek, T. D., Thorngren, D. P., Lopez, E. D., & Ginzburg, S. 2020, ApJ, 893, 36
Kovács, G., Zucker, S., & Mazeh, T. 2002, A&A, 391, 369
Kozai, Y. 1962, AJ, 67, 591
Kurucz, R. L. 1993, SYNTHE spectrum synthesis programs and line data (None) (Cambridge, MA: Smithsonian Astrophysical Observatory)
Levine, S. E., Bida, T. A., Chylek, T., et al. 2012, Proc. SPIE, 8444, 844419
Li, D., Mustill, A. J., & Davies, M. B. 2019a, MNRAS, 488, 1366
Li, J., Tenenbaum, P., Twicken, J. D., et al. 2019b, PASP, 131, 024506
Lidov, M. L. 1962, P&SS, 9, 719
Lin, D. N. C., Bodenheimer, P., & Richardson, D. C. 1996, Natur, 380, 606
Lothringer, J. D., Barman, T., & Koskinen, T. 2018, ApJ, 866, 27
Louden, E. M., Winn, J. N., Petigura, E. A., et al. 2021, AJ, 161, 68
Luhn, J. K., Bastien, F. A., Wright, J. T., et al. 2019, AJ, 157, 149
Lund, M. B., Rodriguez, J. E., Zhou, G., et al. 2017, AJ, 154, 194
Martínez, R. R., Gaudi, B. S., Rodriguez, J. E., et al. 2020, AJ, 160, 111
Mayor, M., & Queloz, D. 1995, Natur, 378, 355
McCully, C., Volgenau, N. H., Harbeck, D.-R., et al. 2018, Proc. SPIE, 10707, 107070K
McLaughlin, D. B. 1924, ApJ, 60, 22
Mészáros, S., Allende Prieto, C., Edvardsson, B., et al. 2012, AJ, 144, 120
Michaud, G., Tarasick, D., Charland, Y., & Pelletier, C. 1983, ApJ, 269, 239
Millholland, S., Wang, S., & Laughlin, G. 2016, ApJL, 823, L7
Millholland, S., Wang, S., & Laughlin, G. 2017, ApJL, 849, L33
Mills, S. M., Howard, A. W., Weiss, L. M., et al. 2019, AJ, 157, 145
Mol Lous, M., & Miguel, Y. 2020, MNRAS, 495, 2994
Morris, R. L., Twicken, J. D., Smith, J. C., et al. 2020, *Kepler* Data Processing Handbook (Moffett Field, CA: NASA Ames Research Center), 87
Morton, T. D., Bryson, S. T., Coughlin, J. L., et al. 2016, ApJ, 822, 86
Naef, D., Latham, D. W., Mayor, M., et al. 2001, A&A, 375, L27
Nagasawa, M., Ida, S., & Bessho, T. 2008, ApJ, 678, 498
Narita, N., Fukui, A., Kusakabe, N., et al. 2019, JATIS, 5, 015001
Narita, N., Sato, B., Hirano, T., & Tamura, M. 2009, PASJ, 61, L35
Newton, E. R., Mann, A. W., Tofflemire, B. M., et al. 2019, ApJL, 880, L17
Parmentier, V., & Crossfield, I. J. M. 2018, Exoplanet Phase Curves: Observations and Theory (Berlin: Springer), 116
Parmentier, V., Line, M. R., Bean, J. L., et al. 2018, A&A, 617, A110
Parviainen, H., Tingley, B., Deeg, H. J., et al. 2019, A&A, 630, A89
Paxton, B., Bildsten, L., Dotter, A., et al. 2011, ApJS, 192, 3
Paxton, B., Cantiello, M., Arras, P., et al. 2013, ApJS, 208, 4
Paxton, B., Marchant, P., Schwab, J., et al. 2015, ApJS, 220, 15
Paxton, B., Schwab, J., Bauer, E., et al. 2018, ApJS, 234, 34
Paxton, B., Smolec, R., Schwab, J., et al. 2019, ApJS, 243, 10
Pepe, F., Mayor, M., Queloz, D., et al. 2004, A&A, 423, 385
Perruchot, S., Bouchy, F., Chazelas, B., et al. 2011, Proc. SPIE, 8151, 815115
Perruchot, S., Kohler, D., Bouchy, F., et al. 2008, Proc. SPIE, 7010, 70140J
Perryman, M. A. C., Brown, A. G. A., Lebreton, Y., et al. 1998, A&A, 331, 81
Petersburg, R. R., Ong, J. M. J., Zhao, L. L., et al. 2020, AJ, 159, 187
Piskunov, N. E., Kupka, F., Ryabchikova, T. A., Weiss, W. W., & Jeffery, C. S. 1995, A&AS, 112, 525
Plavchan, P., Barclay, T., Gagné, J., et al. 2020, Natur, 582, 497
Preston, G. W. 1974, ARA&A, 12, 257
Reffert, S., Bergmann, C., Quirrenbach, A., Trifonov, T., & Künstler, A. 2015, A&A, 574, A116
Renson, P., Gerbaldi, M., & Catalano, F. A. 1991, A&AS, 89, 429
Renson, P., & Manfroid, J. 2009, A&A, 498, 961
Ricker, G. R., Winn, J. N., Vanderspek, R., et al. 2015, JATIS, 1, 014003
Ritter, A., Hyde, E. A., & Parker, Q. A. 2014, PASP, 126, 170
Rodriguez, J. E., Vanderburg, A., Zieba, S., et al. 2020, AJ, 160, 117
Rodríguez Martínez, R., Gaudi, B. S., Rodriguez, J. E., et al. 2020, AJ, 160, 111
Rogers, L. A. 2015, ApJ, 801, 41
Rossiter, R. A. 1924, ApJ, 60, 15
Ryabchikova, T., Piskunov, N., Kurucz, R. L., et al. 2015, PhyS, 90, 054005
Saffe, C., Miquelarena, P., Alacoria, J., et al. 2020, A&A, 641, A145
Saffe, C., Miquelarena, P., Alacoria, J., et al. 2021, A&A, 647, 49
Schlafly, E. F., & Finkbeiner, D. P. 2011, ApJ, 737, 103
Shporer, A. 2017, PASP, 129, 072001
Shporer, A., Wong, I., Huang, C. X., et al. 2019, AJ, 157, 178
Siverd, R. J., Brown, T. M., Barnes, S., et al. 2018b, Proc. SPIE, 10702, 107026C
Siverd, R. J., Brown, T. M., Barnes, S., et al. 2018c, AJ, 155, 35
Siverd, R. J., Collins, K. A., Zhou, G., et al. 2018a, AJ, 155, 35
Smith, J. C., Stumpe, M. C., Van Cleve, J. E., et al. 2012, PASP, 124, 1000
Sneden, C. 1973, ApJ, 184, 839
Sozzetti, A., Damasso, M., Bonomo, A. S., et al. 2021, A&A, 648, 75
Sozzetti, A., Torres, G., Charbonneau, D., et al. 2007, ApJ, 664, 1190
Stangret, M., Pallé, E., Casasayas-Barris, N., et al. 2021, A&A, 654, 73
Stassun, K. G., Oelkers, R. J., Paegert, M., et al. 2019, AJ, 158, 138
Stassun, K. G., & Torres, G. 2018, ApJ, 862, 61
Stumpe, M. C., Smith, J. C., Catanzarite, J. H., et al. 2014, PASP, 126, 100
Stumpe, M. C., Smith, J. C., Van Cleve, J. E., et al. 2012, PASP, 124, 985
Talens, G. J. J., Justesen, A. B., Albrecht, S., et al. 2018, A&A, 612, A57
Talens, G. J. J., Spronck, J. F. P., Lesage, A. L., et al. 2017, A&A, 601, A11
Tanaka, H., Takeuchi, T., & Ward, W. R. 2002, ApJ, 565, 1257
Telting, J. H., Avila, G., Buchhave, L., et al. 2014, AN, 335, 41
Temple, L. Y., Hellier, C., Albrow, M. D., et al. 2017, MNRAS, 471, 2743
Teske, J., Díaz, M. R., Luque, R., et al. 2020, AJ, 160, 96
Thorngren, D., & Fortney, J. 2018, AJ, 155, 214
Tinetti, G., Drossart, P., Eccleston, P., et al. 2018, ExA, 46, 135
Tinney, C. G., Butler, R. P., Marcy, G. W., et al. 2001, ApJ, 551, 507
Torres, G., Fischer, D. A., Sozzetti, A., et al. 2012, ApJ, 757, 161

Triaud, A. H. M. J., Collier Cameron, A., Queloz, D., et al. 2010, A&A, 524, A25
Trifonov, T., Reffert, S., Tan, X., Lee, M. H., & Quirrenbach, A. 2014, A&A, 568, A64
Tsantaki, M., Andreasen, D. T., Teixeira, G. D. C., et al. 2018, MNRAS, 473, 5066
Twicken, J. D., Catanzarite, J. H., Clarke, B. D., et al. 2018, PASP, 130, 064502
Twicken, J. D., Clarke, B. D., Bryson, S. T., et al. 2010, Proc. SPIE, 7740, 774023
Valenti, J. A., & Fischer, D. A. 2005, ApJS, 159, 141
Vogt, S. S., Wittenmyer, R. A., Butler, R. P., et al. 2010, ApJ, 708, 1366
von Essen, C., Mallonn, M., Borre, C. C., et al. 2020, A&A, 639, A34
Wakeford, H. R., Visscher, C., Lewis, N. K., et al. 2017, MNRAS, 464, 4247
Wang, S., Jones, M., Shporer, A., et al. 2019, AJ, 157, 51
Ward, W. R. 1997, Icar, 126, 261
Weiss, L. M., Fabrycky, D. C., Agol, E., et al. 2020, AJ, 159, 242
Winn, J. N., Fabrycky, D., Albrecht, S., & Johnson, J. A. 2010, ApJL, 718, L145
Winn, J. N., Holman, M. J., Torres, G., et al. 2008, ApJ, 683, 1076
Winn, J. N., Johnson, J. A., Albrecht, S., et al. 2009, ApJL, 703, L99
Wittenmyer, R. A., Butler, R. P., Horner, J., et al. 2020, MNRAS, 491, 5248
Wittenmyer, R. A., Clark, J. T., Zhao, J., et al. 2019, MNRAS, 484, 5859
Wittenmyer, R. A., Jones, M. I., Horner, J., et al. 2017, AJ, 154, 274
Wong, I., Benneke, B., Shporer, A., et al. 2020a, AJ, 159, 104
Wong, I., Shporer, A., Daylan, T., et al. 2020c, AJ, 160, 155
Wong, I., Shporer, A., Kitzmann, D., et al. 2020b, AJ, 160, 88
Wright, J. T., Marcy, G. W., Butler, R. P., et al. 2008, ApJL, 683, L63
Xiang, M.-S., Rix, H.-W., Ting, Y.-S., et al. 2020, ApJ, 898, 28
Yi, S., Demarque, P., Kim, Y.-C., et al. 2001, ApJS, 136, 417
Zhou, G., Bakos, G. Á., Bayliss, D., et al. 2019b, AJ, 157, 31
Zhou, G., Huang, C. X., Bakos, G. Á., et al. 2019a, AJ, 158, 141
Zhou, G., Rodriguez, J. E., Collins, K. A., et al. 2016, AJ, 152, 136
Zinnecker, H., & Yorke, H. W. 2007, ARA&A, 45, 481